Numerical Modelling of Pipeline Scour under the Combined Action of Waves and Current with Free-Surface Capturing

Nadeem Ahmad[a,1], Hans Bihs[a], Dag Myrhaug[b], Arun Kamath[a], Øivind A. Arntsen[a]

[a] *Department of Civil and Environmental Engineering, Norwegian University of Science and Technology, 7491 Trondheim, Norway.*

[b] *Department of Marine Technology, Norwegian University of Science and Technology, Trondheim, 7491, Norway*

Abstract

Understanding the pipeline scour processes under the combined action of waves and current is essential for adequate scour protection measures. This paper presents the numerical modelling of pipeline scour under the co-directional combined action of waves and current including the prediction of the unsteady free surface. The numerical modelling is performed with the open-source CFD model REEF3D. The model solves the Reynolds-Averaged Navier-Stokes (RANS) equations together with the $k-\omega$ turbulence model and a sediment transport algorithm. In order to ensure the accuracy of the flow field, the model is thoroughly validated for the hydrodynamics of co-directional combined waves and current. Results for the velocity profiles show a good agreement with the experimental observations. The model is then applied to simulate the different case scenarios of the scour under waves alone, current alone, and combined waves and current. The numerical results for scour below the pipeline show good agreement with the experimental data which confirms the applicability of the model to study pipeline scour under the combined action of waves and current. A series of simulations are run for different values of the non-dimensional parameter for the combined waves and current U_{cm} varying between 0 to 1.0 for the given KC number. The results demonstrate the correlation between values of U_{cm} and (1) the flow field below the pipeline, (2) the scour depth, and (3) the temporal variation of the scouring process. The findings highlight the variation of the maximum scour depth below the pipeline with U_{cm}.

Keywords: pipeline scour, wave-current interaction, free surface, numerical wave tank, CFD.

[1] Corresponding Author, Email: nadeem.ahmad@ntnu.no, Ph: (+47) 93 97 91 60, Fax: (+47) 73 59 70 21

1. Introduction

The pipelines in shallow water near the coastline are exposed to the combined action of waves and current. This results in a scour hole with a bowl-shaped depression below the pipeline. When the extent of the scour becomes larger, the pipeline starts to sag, resulting in lateral instability and possible leakages. Therefore, it remains crucial to investigate pipeline scour to extend the relevant knowledge and numerical scour modelling capabilities.

There are several experimental studies investigating pipeline scour in the current literature, e.g. [1, 2, 3, 4, 5, 6]. The important aspects of pipeline scour, such as the critical condition for the onset of scour, the tunnel scour, the lee-wake scour, the impact of the lee-wake on pipeline scour due to steady current, the effect of Keulegan-Carpenter number (KC = $U_m T/D$, where U_m is the maximum horizontal wave particle velocity at the bottom, and T is the wave period), the influence of the Shields parameter, scour around multiple pipelines and the effect of the gap between the seabed and the pipeline are presented as novel elements of the pipeline scouring process. However, these studies have only focused on the pipeline scour under either waves or steady current conditions. The scour below the pipeline under the combined action of waves and current is further complicated and only a few studies have discussed the issue. Lucassen [7] performed a series of experiments and found that the maximum scour depth below the pipeline (S/D) increases with the non-dimensional parameter for the combined action of waves and current $U_{cm} = u_c/(u_c + u_m)$, where u_m is the maximum horizontal wave particle velocity and u_c is the steady current velocity. The term $U_{cm} = 0$ denotes waves alone and $U_{cm} = 1$ a steady current condition. Sumer and Fredsøe [8] investigated pipeline scour under the combined action of waves and current. In their experiments, they observed that for a given KC number, S/D decreases for $U_{cm} < 0.50$ and shows an increase in S/D for $U_{cm} > 0.50$. Myrhaug et al. [9] obtained an engineering approach based on existing experimental data by which the scour depth below the pipeline for combined random waves and current, the second-order Stokes wave theory is used for wave modelling by assuming the basic harmonic wave motion to be a stationary Gaussian narrow-band random process. Also, the effects of second-order wave asymmetry are included.

Various numerical investigations have been performed to study pipeline scour using numerical models. Brørs [10] analyzed pipeline scour under a steady current by solving the incompressible Reynolds-Averaged Navier-Stokes (RANS) equations with the $k - \epsilon$ turbulence model and a morphological solver. The study focussed on steady flow around a pipeline and the resulting scour with the free surface modelled as a rigid lid. Li and Cheng [11] investigated pipeline scour

using large eddy simulations (LES) in terms of the bed shear stress. The equilibrium scour profile was retrieved using an iterative method based on the assumption that the equilibrium seabed shear stress is equal to the critical shear stress without using Exner's continuity equation for the bed changes. Liang et al. [12] studied numerical modelling of time-dependent local scour below a pipeline subjected to a steady current. The numerical results showed scour in the clear-water and live-bed scour regimes. In their follow-up study, Liang and Cheng [13] presented numerical modelling of pipeline scour for waves alone. A source of uncertainty was found in the representation of the wave motion, as a simplified oscillatory flow without free surface calculation was used. Fuhrman et al. [14] investigated pipeline scour under waves with a RANS-based numerical model and found that the backfilling process is characterized by an initial re-distribution phase involving re-organization of sediments in the immediate vicinity of the pipeline. In their study, the wave motion was specified as a simplified oscillatory flow and the free surface was not resolved. Liu et al. [15] investigated wave-induced scour around pipelines. Instead of simplified oscillatory flow, the wave motion was handled using a non-linear wave model. The study concluded the necessity of utilising the free surface to study local scour around pipelines using the Arbitrary Lagrangian-Eulerian (ALE) method.

Numerical modelling of scour below pipelines exposed to the combined action of waves and current is limited to a few studies. Hansen [16] presented modelling of the scouring process under the combined action of waves and current using a potential flow model. He concluded that the scour depth decreases with an increasing steady current velocity. However, the study is limited to lower values of U_{cm} in the range of 0 to 0.3. The usage of a potential flow model is a limitation of the study, since it cannot resolve the lee-wake flow and consequently cannot predict the lee-wake scour. Larsen et al. [17] studied pipeline scour under the combined action of waves and current by modelling the wave motion as a simplified oscillatory flow with a steady flow condition. The study investigated pipeline scour for different values of U_{cm} by scaling-down the pipeline diameter and maintaining the Shields similarity parameter. In their study, no free surface calculations were performed and the free surface was modelled as a rigid lid. Despite the existing research, there is still a need for further discussion on pipeline scour under the combined action of waves and current including (1) the representation of the wave motion using higher-order non-linear wave motion, (2) validation of the hydrodynamics of the combined action of waves and current prior to the sediment transport calculations and (3) the change in the bed elevation including free surface capturing without scaling of the experimental data.

The main objective of the present paper is to investigate the scour below a pipeline exposed

to the combined action of waves and current together with the simulation of the actual free surface dynamics. The study discusses the accurate generation and propagation of the second-order Stokes waves in the numerical wave tank (NWT). In order to ensure the quality of the wave hydrodynamics in the NWT, the validation is performed for the combined action of waves and current. The numerical results show a close match with the wave theory and the experimental data from Umeyama [18]. The model is then validated for pipeline scour. Further simulations are run to evaluate pipeline scour under waves and steady current conditions. The numerical results show good agreement with the experimental data from Sumer and Fredsøe [8] and Mao [1] for pipeline scour under waves and current conditions. Finally, the validated model is applied to simulate the pipeline scour under the combined action of waves and current for different values of U_{cm} for given KC numbers. The numerical results examine in depth how the change in U_{cm} contributes to the flow hydrodynamics and consequently the scour below the pipeline exposed to the combined action of waves and current. The present study gives new insight into the mechanics of scour due to the combined effects of waves and current by including the free surface.

2. Numerical Model

The open-source CFD model REEF3D [19, 20] is selected for the numerical modelling of scour below pipelines. The model has been successfully used for wave-structure interaction problems [21, 22, 23], wave-induced scour around vertical piles [24, 25], and local scour problems in coastal areas [26]. An overview of the different modules and the governing equations used to simulate the flow hydrodynamics, the free surface and the morphological development is given here.

2.1. Hydrodynamic model

The flow field in the NWT is calculated by solving the incompressible Reynolds-Averaged Navier-Stokes (RANS) equations, along with the continuity equation as given in Eqs. (1) and (2), respectively:

$$\frac{\partial u_i}{\partial x_i} = 0 \tag{1}$$

$$\frac{\partial u_i}{\partial t} + u_j \frac{\partial u_i}{\partial x_j} = -\frac{1}{\rho}\frac{\partial p}{\partial x_i} + \frac{\partial}{\partial x_j}\left[(\nu + \nu_t)\left(\frac{\partial u_i}{\partial x_j} + \frac{\partial u_j}{\partial x_i}\right)\right] + g_i \tag{2}$$

where u_i is the fluid velocity, p is the pressure, ρ is the fluid density, ν is the fluid kinematic viscosity, ν_t is the eddy-viscosity, and g is the gravitational acceleration. The k-ω model [27] is

used as closure for the RANS equations to calculate the eddy-viscosity. Large velocity gradients around the free surface cause overproduction of turbulence which can lead to artificial damping of the free surface dynamics [28, 29, 30]. Close to the free surface, the components normal to the free surface are supressed and the components parallel to the surface are enhanced as suggested by Naot and Rodi [28]. By prescribing a specific turbulence dissipation term at the free surface ω_s, these physics can be accurately represented in the numerical model:

$$\omega_s = \frac{c_\mu^{-\frac{1}{4}}}{\kappa} k^{\frac{1}{2}} \left(\frac{1}{y'} + \frac{1}{y*} \right) \tag{3}$$

where $c_\mu = 0.07$, $k = 0.40$ is the von Karman constant, $y' = 0.07$ * h, is the virtual origin of the turbulent length scale [31], h is water depth, and y is the distance from the nearest wall to give a smooth transition of ω from the free surface value to the rough-wall boundary. The damping around the interface is activated by using the Dirac delta function $\delta(\phi)$:

$$\delta(\phi) = \begin{cases} \frac{1}{2\epsilon} \left(1 + \cos\left(\frac{\Pi\phi}{\epsilon} \right) \right) & if \ \ |\phi| < \epsilon \\ 0 & else \end{cases} \tag{4}$$

where $\epsilon = 1.6dx$ is the width over which the delta function is applied and dx is the grid size. The value of ϵ is chosen in such a way that minimum one grid cell is involved around the interface in each direction. Further details of the governing equations can be found in Bihs et al. [19].

The spatial derivatives are approximated using advanced finite difference methods on a Cartesian grid. The convective terms of the RANS equations are discretized with the fifth-order accurate conservative Weighted Essential Non-Oscillatory (WENO) scheme [32]. The time step for the transient flow is determined using the adaptive time stepping method. In this method, the time step is controlled with the Courant-Friederichs-Lewy (CFL) number [33], which takes the influence of the velocity, diffusion, and source terms such as the acceleration due to the gravity into account. The pressure is treated with the projection method [34]. The BiCGStab [35] solver from the high-performance solver package HYPRE with the semi-coarsening multi-grid preconditioner PFMG [36] is implemented to solve the Poisson equation for the pressure.

2.2. Free surface model

The free surface is calculated with the level set method [37]. This method describes the interface between two phases implicitly using a continuous signed distance function $\phi(\vec{x}, t)$. The free surface is calculated as the zero level set of $\phi(\vec{x}, t)$, while phase 1 and phase 2 are defined

as the positive and negative level set of $\phi(\vec{x},t)$ as follows:

$$\phi(\vec{x},t)\begin{cases} > 0 & if\ \vec{x}\ is\ in\ phase\ 1 \\ = 0 & if\ \vec{x}\ is\ at\ the\ interface \\ < 0 & if\ \vec{x}\ is\ in\ phase\ 2 \end{cases} \tag{5}$$

The signed distance function $\phi(\vec{x},t)$ satisfies the Eikonal equation, i.e., $|\nabla\phi(\vec{x},t)| = 1$ in the whole domain. The evolution of the free surface over time is calculated with the convection equation:

$$\frac{\partial\phi}{\partial t} + u_j\frac{\partial\phi}{\partial x_j} = 0 \tag{6}$$

where u_j is the fluid velocity calculated from the solution of the RANS-equations. The convective terms of the level set function are discretized with the Hamilton-Jacobi formulation of the WENO scheme [38]. A third-order TVD Runge-Kutta time scheme [39] is used for time treatment. As the free surface evolves, the level set function $\phi(\vec{x},t)$ loses its signed distance property and is therefore reinitialised each time step [40].

2.3. Morphological model

The calculation of the scouring process is based on the fundamental theory of sediment transport which states that water flowing over a sediment bed results in the incipient motion of the sediment particles when the acting bed shear stress τ is higher than the critical bed shear stress τ_c. The morphological model covers the calculation of the bed shear stress, the bed-load, the suspended-load and the change of bed elevation. Details of the morphological model are described in Ahmad et al. [25] and a short description of the relevant equations is presented here. The bed shear stress τ due to the flow velocity is determined considering a logarithmic velocity profile near the bed as:

$$\tau = \rho u_*^2 \tag{7}$$

where $u_* = u\ \kappa/ln\ (\frac{30z}{k_s})$ is the shear velocity, u is the velocity at a height z above the bed, calculated from the RANS-equations, $\kappa = 0.4$ is the von Karman constant, $k_s = 3d_{50}$ is the equivalent sand roughness and d_{50} is the median grain size. The bed-load transport rate $q_{b,i}$ calculations are made with the formulation proposed by van Rijn [41]:

$$\frac{q_{b,i}}{d_{50}^{1.5}\sqrt{(s-1)g}} = 0.053\ \frac{T^{2.1}}{D_*^{0.3}} \tag{8}$$

where $T = \frac{\tau - \tau_{cr}}{\tau_{cr}}$ is the transport stage parameter, $D_* = d_{50}\left[\frac{(s-1)g}{\nu^2}\right]^{1/3}$ is the dimensionless grain size, $s = \rho_s/\rho$ is the specific density, ρ_s is the sediment density and ρ is the water density, $\tau_{cr} = r\ \tau_0$ is the modified critical bed shear stress, τ_0 is the critical bed shear stress on a horizontal bed which is calculated using the Shields diagram and r is the modification factor to account for the effect of the sloping bed. The modification factor r is calculated using the formulation suggested by Dey [42]. The effect of the sloping bed is accounted for by considering the longitudinal bed slope θ, the transverse bed slope β, the angle of repose of the sediment φ and the drag and lift forces as:

$$r = \frac{1}{\left(1 - \eta \tan\varphi\right)\tan\varphi}\Big\{-\left(\sin\theta + \eta\tan^2\varphi\sqrt{\cos^2\theta - \sin^2\beta}\right) + \Big[\left(\sin\theta + \eta\tan^2\varphi\sqrt{\cos^2\theta - \sin^2\beta}\ \right)^2 + \left(1 - \eta^2\tan^2\varphi\right)\left(\cos^2\theta\tan^2\varphi - \sin^2\beta\tan^2\varphi - \sin^2\theta - \sin^2\beta\right)\Big]^{0.5}\Big\} \tag{9}$$

where η is the ratio of the drag force to the inertia force. Thus, the value of the critical bed shear stress τ_{cr} is calculated to be lower for downhill slopes and higher for uphill slopes compared to τ_0. The suspended sediment load is calculated using a convection-diffusion equation. Details of the equations used for the suspended-load and numerical treatment can be found in Ahmad et al. [25]. An important feature of the morphological bed changes is that the sides of the scour hole fail when the bed slope exceeds the angle of repose (φ). This is accounted for by using a sand slide algorithm in the sediment transport model. A correction factor of -2° is applied in an iterative manner to redistribute excess sediment if the bed slope exceeds the angle of repose (φ) [43, 44]. It is observed that the downhill bed slope is expected to be larger than the uphill bed slope [45]. Therefore, for this study, the modified angle of repose for the downhill slope is assumed to be $\varphi = 45°$, and for the uphill bed slope, $\varphi = 35°$, depending on the bed velocity vector orientation relative to the bed slope [46]. The change in bed elevation is calculated with Exner's formula. The method is based on the conservation of sediment mass where the spatial variation in the bed-load is conserved with the temporal change in the vertical bed elevation. The morphological evolution occurs as a non-linear propagation of the bed-level deformation in the direction of the sediment transport. The transient change in bed level is defined as follows:

$$\frac{\partial z_b}{\partial t} + \frac{1}{(1-n)}\ \left[\ \frac{\partial q_{b,x}}{\partial x}\ \right] + E - D = 0 \tag{10}$$

Here, z_b is the bed-level, $q_{b,x}$ is the bed-load in the x-direction and n is the sediment porosity.

The term $(E-D)$ defines the net flux of sediment across the interface between the bed-load and the suspended load and is calculated using the formula by Wu et al. [47]. The bed topography is represented with the level set method, which implicitly defines the sediment bed as the zero level set. The driving factor is $\partial z_b/\partial t$ which transforms the interface in the vertical direction due to erosion or deposition.

3. Results discussion

3.1. Hydrodynamic validation

This section describes the validation of the model to simulate the flow under the combined action of waves and current. At first, the simulations are run without steady current, i.e. waves alone for different values of wave steepness. The velocity profiles are compared with the observations from the experiments [18]. The combined action of waves and current is then simulated by adding the steady current component. The simulated velocity profiles are plotted for different values of U_{cm} and are compared with the experimental data [18].

3.1.1. Computational setup and boundary conditions

The computational setup is similar to the experimental setup used by Umeyama [18]. The experimental flume is 25.0 m long, 0.7 m wide and 1.0 m deep with a still water depth of $h = 0.30$ m and a wave period $T = 1.0$ s for all the experiments. The simulations are performed in an 8.8 m long and 1.0 m high 2D NWT without structures. Based on the incident wave characteristics, second-order Stokes wave theory is chosen for the wave generation in the NWT corresponding to the experiments. The boundary conditions of the NWT are as follows: The waves generation from the inlet is based on the Dirichlet type inlet boundary condition where the free surface elevation (η) and incident wave velocity (u, w) are prescribed based on the second-order Stokes wave theory [48] as:

$$\eta(x,z,t) = \frac{H}{2}\cos\theta + \frac{H^2k}{16}\frac{\cosh kh}{\sinh^3 kh}(2+\cosh 2kh)\cos 2\theta \tag{11}$$

$$\Phi(x,z,t) = \frac{Hg}{2\omega}\frac{\cosh k(h+z)}{\cosh kh}\sin\theta + \frac{3}{32}H^2\omega\frac{\cosh 2k(h+z)}{\sinh^4 kh}\sin 2\theta \tag{12}$$

$$u(x,z,t) = \frac{\partial\Phi}{\partial x}; \quad w(x,z,t) = -\frac{\partial\Phi}{\partial z} \tag{13}$$

where η is the free surface elevation, Φ is the velocity potential, H is the incident wave height, T is the wave period, $k = \frac{2\pi}{\lambda}$ is the deep water wave number, λ is the wave length, and $\theta = kx - \omega t$

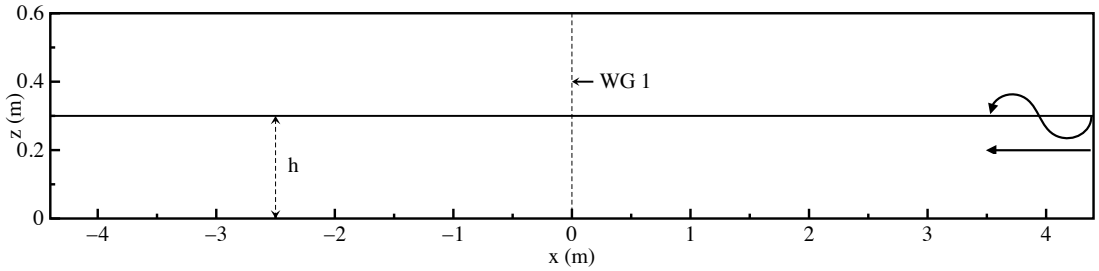

Figure 1: Numerical setup used for the hydrodynamic validation of the co-directional combined waves and current. The flow is generated from right-to-left side of the NWT as in the experiments. Length of NWT is 8.8 m and a wave gauge is located at centre of NWT, $x = 0$ m. Source of the experimental data: Umeyama [18].

is the wave phase. The dispersion relation is defined as $\omega^2 = gk \tanh kh$, where ω is the angular wave frequency and z the vertical coordinate with the origin at the still water depth h. The second-order term in the Eq. (11) and Eq. (12) are directly related to the wave steepness and accounts for the asymmetric nature of the wave. The waves are absorbed at the outlet with the active wave absorption (AWA) method [49]. In this method, the waves reaching the outlet are handled by cancelling out the reflected waves and prescribing the velocity u_o as:

$$u_o = -\sqrt{\frac{g}{h}}\,\eta_r \tag{14}$$

where η_r is the reflected wave amplitude defined as:

$$\eta_r = \eta_m - h \tag{15}$$

Here, η_m is the actual free surface elevation and h is the still water level. Thus the reflected waves from the outlet are absorbed. The advantage of using the AWA method as an outlet boundary condition is that instead of providing a long relaxation zone for wave dissipation, the wave is absorbed directly at the outlet [25]. The other boundary conditions are as follows: The bottom of the NWT is considered as a rough-wall. The sides and the top of the NWT are considered as symmetry planes. The boundary of the pipeline and seabed is defined using the immersed boundary method with the local directional ghost cell approach [50]. A Cartesian grid with $dx = dy = dz$ is used in all the simulations. An overview of the computational domain and boundary conditions are given in Fig. 1. The details of the simulations are summarized in Table 1.

Test	dx	D	CFL	T	H	h	ka	u_m	$u_m/\sqrt{gh}$	u_c	$u_c/\sqrt{gh}$	U_{cm}	θ	KC	S/D	S/D
	(m)	(m)		(s)	(m)	(m)		(m/s)		(m/s)					(Num)	(Exp)
Grid convergence study																
A1	0.04	-	0.25	1.0	0.036	0.30	0.082	0.113	0.066	0	0	0	-	-	-	-
A2	0.03	-	0.25	1.0	0.036	0.30	0.082	0.113	0.066	0	0	0	-	-	-	-
A3	0.02	-	0.25	1.0	0.036	0.30	0.082	0.113	0.066	0	0	0	-	-	-	-
A4	0.01	-	0.25	1.0	0.036	0.30	0.082	0.113	0.066	0	0	0	-	-	-	-
A5	0.005	-	0.25	1.0	0.036	0.30	0.082	0.113	0.066	0	0	0	-	-	-	-
Time convergence study																
B1	0.01	-	0.50	1.0	0.036	0.30	0.082	0.113	0.066	0	0	0	-	-	-	-
B2	0.01	-	0.40	1.0	0.036	0.30	0.082	0.113	0.066	0	0	0	-	-	-	-
B3	0.01	-	0.30	1.0	0.036	0.30	0.082	0.113	0.066	0	0	0	-	-	-	-
B4	0.01	-	0.20	1.0	0.036	0.30	0.082	0.113	0.066	0	0	0	-	-	-	-
B5	0.01	-	0.10	1.0	0.036	0.30	0.082	0.113	0.066	0	0	0	-	-	-	-
Propagation of waves alone																
C1	0.01	-	0.10	1.0	0.010	0.30	0.024	0.031	0.018	0	0	0	-	-	-	-
C2	0.01	-	0.10	1.0	0.023	0.30	0.054	0.072	0.042	0	0	0	-	-	-	-
C3	0.01	-	0.10	1.0	0.036	0.30	0.083	0.113	0.066	0	0	0	-	-	-	-
Combined propagating waves and current																
D1	0.01	-	0.10	1.0	0.009	0.30	0.020	0.028	0.016	0.08	0.047	0.74	-	-	-	-
D2	0.01	-	0.10	1.0	0.020	0.30	0.046	0.063	0.037	0.08	0.047	0.56	-	-	-	-
D3	0.01	-	0.10	1.0	0.030	0.30	0.070	0.094	0.055	0.08	0.047	0.46	-	-	-	-
Pipeline scour under waves alone																
E1	0.01	0.05	0.10	0.90	0.40	0.099	0.050	0.060	0.143	-	-	0	0.06	2	0.18	0.14
E2	0.01	0.05	0.10	1.43	0.40	0.228	0.115	0.110	0.135	-	-	0	0.11	7	0.32	0.26
E3	0.01	0.05	0.10	2.70	0.40	0.209	0.106	0.090	0.053	-	-	0	0.035	11	0.33	0.37
E4	0.01	0.05	0.10	3.13	0.40	0.257	0.130	0.090	0.041	-	-	0	0.06	16	0.36	0.40
E5	0.01	0.05	0.10	3.57	0.40	0.259	0.131	0.110	0.040	-	-	0	0.06	19	0.52	0.43
Pipeline scour under steady current alone																
F1	0.01	0.10	0.10	-	-	0.35	-	-	-	0.350	0.189	1.0	0.06	∞	0.55	0.55
F2	0.01	0.10	0.10	-	-	0.35	-	-	-	0.500	0.270	1.0	0.09	∞	0.70	0.70

Table 1: List of simulations performed for hydrodynamic and morphological validation for the co-directional combined waves and current. Here, ka is the wave steepness, $k = \frac{2\pi}{\lambda}$ is the wave number, $a = H/2$ is the wave amplitude and λ is the wavelength. Test series A1-D3 corresponds to hydrodynamic validation. In these tests, flow is generated from right-to-left as in the experiments from Umeyama [18]. The experimental data for test (E1-E5) conducted for the pipeline scour under waves [3] and test F1-F2 is conducted for the pipeline scour steady current [1]. For these simulations (E1-F2), the waves and current are generated from left-to-right as in the experiments from Sumer and Fredsøe [3] and Mao [1].

3.1.2. Grid and time convergence study

At first, grid and time step convergence tests are performed. The purpose of the tests is to ensure that the quality of the waves generated in the NWT is independent of the computational mesh. One wave gauge $WG1$ is fixed at the center of the NWT, where the pipeline is located

in the scour simulations. The simulations are carried out for the steepest wave analyzed in the experiments [18], with wave steepness $ka = 0.083$. Five different grid sizes, $dx = 0.04$ m, 0.03 m, 0.02 m, 0.01 m, and 0.005 m are tested. For all values of dx, the CFL number is 0.25. The simulations are run for $t/T = 50$. The accuracy of the simulated wave is analyzed by a comparison between the simulated wave elevations and the wave theory. Figs. 2(a-e) show sequences of the simulated wave free surface elevations versus t/T. It is found that the wave

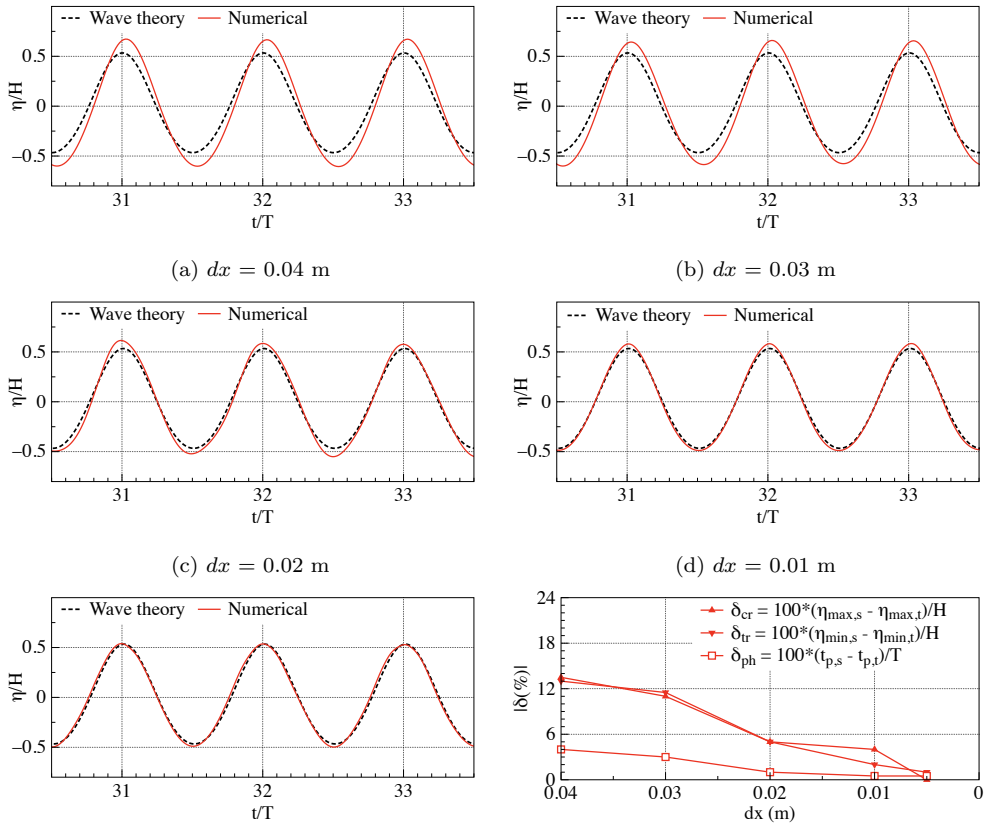

(a) $dx = 0.04$ m (b) $dx = 0.03$ m

(c) $dx = 0.02$ m (d) $dx = 0.01$ m

(e) $dx = 0.005$ m (f) Wave accuracy plotted against dx

Figure 2: Grid convergence study of the wave field generated in a NWT without the pipeline. The total duration of the simulation run is $t/T = 50$. Wave elevation is measured at WG1. The plots depict a comparison between the simulated free surface elevations and the wave theory for different grid sizes. Test conditions are: The wave steepness, $ka = 0.082$, the wave period $T = 1.0$ s, CFL = 0.25. Here δ_{cr}, δ_{tr}, and δ_{ph} refers to the discrepancy in wave crests, wave troughs, and wave phases, respectively. $\eta_{max,s}$ is the simulated wave crest, $\eta_{max,t}$ is the theoretical wave crest, $\eta_{min,s}$ is the simulated wave trough, $\eta_{max,t}$ is the theoretical wave trough, $t_{p,s}$ is the simulated wave crest time and $t_{p,s}$ is the theoretical wave crest time. The red solid line: numerical result; black dotted line: Second-order Stokes wave theory.

elevations are over-predicted on coarser grids, but the agreement is seen to be improving with

decreasing grid size dx. Fig. 2(f) shows the accuracy of the simulated wave, which is quantified in terms of the difference (δ) of the simulated wave elevations and the wave phase from the corresponding wave theory. The term δ is defined in Fig. 2(f). For the coarse grid $dx = 0.04$ m, the simulated crests and troughs of the wave show an about 13% over-prediction, which decreases to $\delta = 2\%$ when the grid size is reduced to $dx = 0.005$ m. The simulated wave phase shows a relatively close agreement with the wave theory. The difference between the simulated and theoretical wave phase is found to decrease from 4% to 1% as the grid size is reduced from $dx = 0.04$ m to 0.005 m.

Fig. 3 shows the results of the time convergence study. In this case, the grid size is maintained

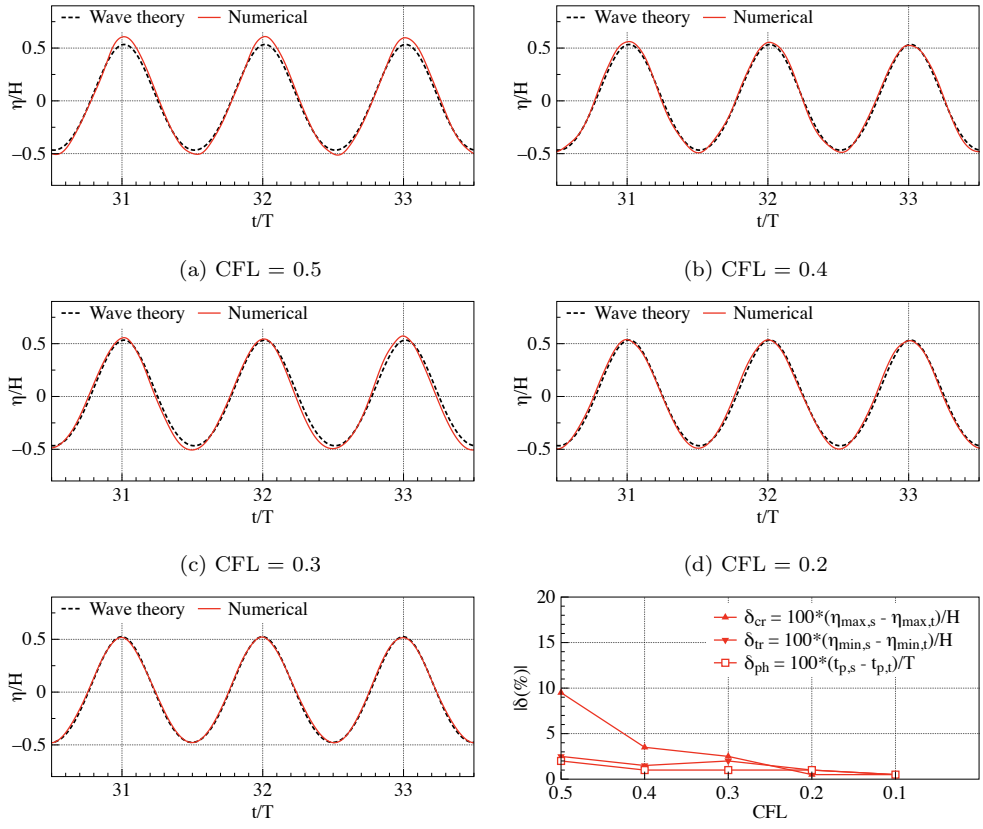

(a) CFL = 0.5 (b) CFL = 0.4

(c) CFL = 0.3 (d) CFL = 0.2

(e) CFL = 0.1 (f) Wave accuracy plotted against the CFL number

Figure 3: Time convergence study of the wave field generated in a NWT. The total duration of the simulation run is $t/T = 50$. The wave elevation is measured at WG1. The plots depict a comparison between the simulated free surface elevations and the wave theory for different CFL numbers. Test conditions are: The wave steepness, $ka = 0.082$, the wave period $T = 1.0$ s, $dx = 0.01$. The red solid line: numerical result; black dotted line: Second-order Stokes wave theory.

as $dx = 0.01$ m for all simulations. The calculation of the transient flow is based on adaptive time stepping where the time step is calculated based on the CFL number. Therefore, instead of testing a fixed time step, different values of the CFL number, i.e. CFL = 0.50, 0.40, 0.30, 0.20 and 0.10 are tested. The other test conditions are the same as used in the grid convergence study. Figs. 3(a-e) show the simulated wave elevations for different CFL numbers. For CFL = 0.50, the simulated crests of the wave are found to be 10% over-predicted. The difference between the simulated wave and the wave theory is reduced to 0.5% when the CFL number is decreased to CFL = 0.10. The simulated troughs and the phase of the wave are in close agreement with the wave theory. For the CFL number range of 0.5 to 0.2, the difference between the simulated result and wave theory range 3% to 0.5%. The accuracy of the numerical results is seen to be the same when CFL is further reduced to 0.10. Thus, the solution is considered to be converged at CFL = 0.10 with the grid size of $dx = 0.01$ m and is therefore maintained in the following numerical simulations.

3.1.3. Kinematics of waves alone

The correct representation of the wave kinematics in the NWT is verified in this section. The simulations are run for different values of wave steepness $ka = 0.024$, 0.054 and 0.083. The steady current velocity is $u_c/\sqrt{gh} = 0$ for all simulations, i.e., $U_{cm} = 0$ (waves alone).

Fig. 4 shows the sequence of the wave velocity profiles plotted at intervals of $t/T = 0.25$. The velocity profiles are measured below the wave trough level. The wave interval $t/T = 0$ and $t/T = 0.50$ correspond to the wave trough and wave crest, respectively. Fig. 4(a) shows the development of the velocity profile for the wave steepness ka =0.024. It is seen that the velocity varies between $u/\sqrt{gh}$ = -0.02 and 0.02 corresponding to the trough and crest of the waves. Figs. 4(b-c) depict the velocity profiles when the wave steepness is increased to ka = 0.054 and ka =0.083, respectively. While the same pattern is seen, the velocity $u/\sqrt{gh}$ varies between -0.05 and 0.05 for $ka = 0.054$, and between -0.07 and 0.07 for $ka = 0.083$. It appears that the predicted velocity profiles agree well with the experimental data [18].

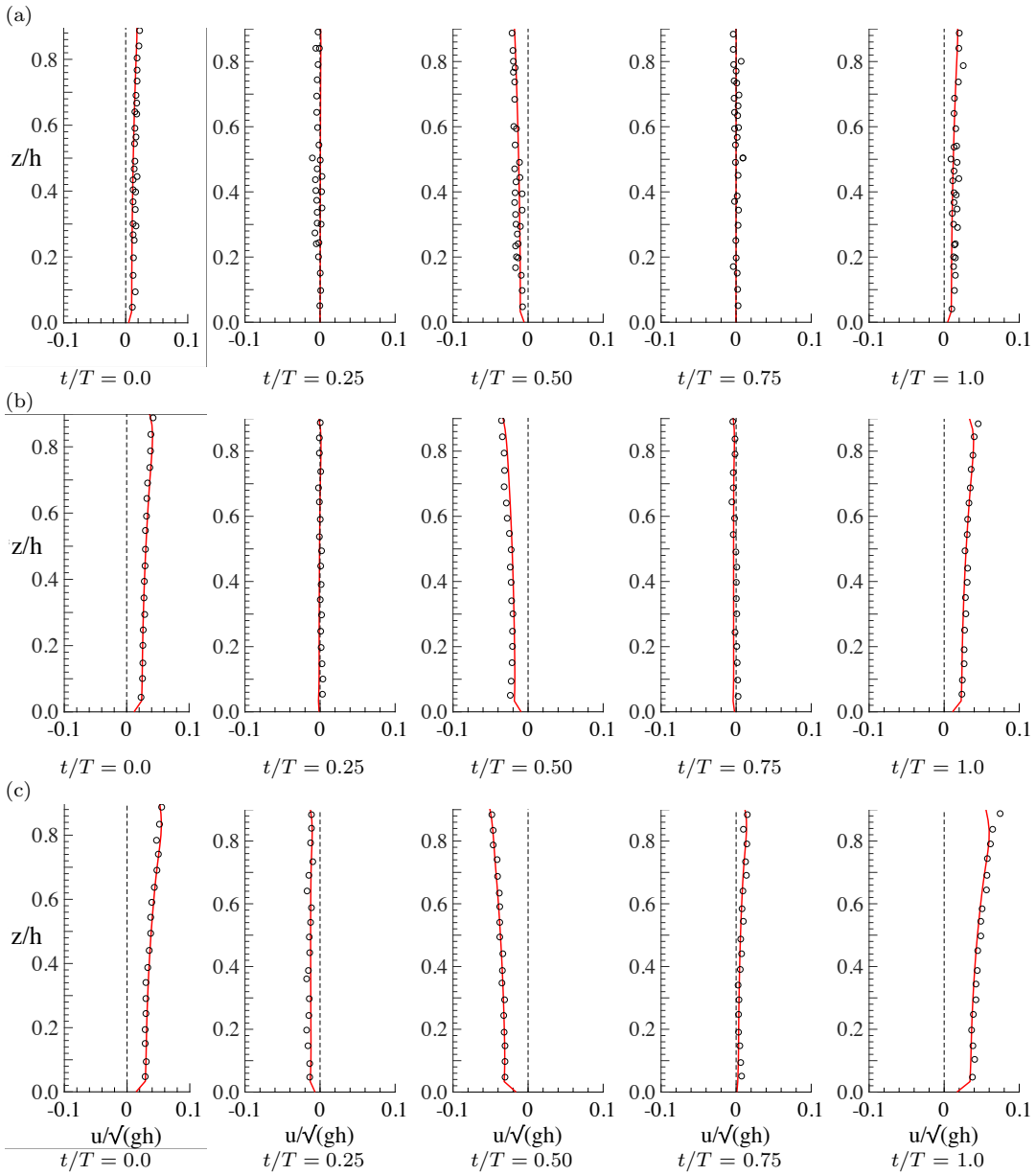

Figure 4: Simulated velocity profiles of the wave for different values of wave steepness ka = (a) 0.024, (b) 0.056, (c) 0.083. The other test conditions are: Wave period T = 1.0 s, grid size dx = 0.01 m, CFL = 0.10 and the wave gauge WG1 location is x = 0 m, see also Table 1. The red solid line: simulated result; black circles: the experimental data from Umeyama [18].

3.1.4. Kinematics of the co-directional combined waves and current

Fig. 5 depicts the velocity profiles when the waves are combined with a steady current. The simulations are run for different values of U_{cm} for the wave steepnesses ka = 0.020, 0.046, and

0.070. The steady current velocity is $u_c/\sqrt{gh}$ = -0.047 for all simulations. The negative sign of the steady current velocity indicates the flow direction from right-to-left. The waves also advance in the same direction, this means the velocity under the wave crest and wave trough are negative and positive, respectively as in the experiments [18]. The other test conditions are the same as in the previous validation cases, see Table 1.

Fig. 5(a) shows the sequences of velocity profiles for $U_{cm} = 0.74$, when a wave of steepness ka = 0.023 is combined with a steady current of $u_c/\sqrt{gh}$ = -0.047. It is found that the interaction of the waves with a steady current leads to an asymmetric wave profile. In comparison to the current velocity, the velocity decreases to $u/\sqrt{gh}$ = -0.040 at $t/T = 0$ corresponding to the wave trough. This is due to that the wave opposes the steady current. The velocity increases to $u/\sqrt{gh}$ = -0.06 beneath the wave crest at $t/T = 0.50$. This increase in the velocity is attributed to that the steady current intensifies the wave motion beneath the wave crest. The simulated sequence of the velocity profiles is consistent with the experiments [18]. Fig. 5(b) shows the sequence of the velocity profiles for $U_{cm} = 0.56$, when the wave steepness is increased to $ka = 0.046$. The velocity is seen to be almost zero close to the free surface at t/T=0. This corresponds to the condition of wave blocking where the velocity beneath the wave trough matches the current velocity and blocks the wave motion. However, the velocity close to the bottom is seen to be $u/\sqrt{gh}$ = -0.02 which indicates a flow in the current direction. The velocity increases to $u/\sqrt{gh}$ = -0.10 under the wave crest at $t/T = 0.50$. Fig. 5(c) shows the velocity profiles for $U_{cm} = 0.46$ when the wave steepness is increased to $ka = 0.083$. It is seen that under the wave trough, the velocity profile shows a reverse flow close to the free surface with the velocity $u/\sqrt{gh} = 0.02$ and a decrease in the velocity to $u/\sqrt{gh}$ = -0.02 close to the bottom. The velocity decreases to $u/\sqrt{gh}$ = -0.12 under the wave crest. The numerical results show that a successive increase in wave steepness leads to an increase in the velocity magnitude under the wave crest and decrease in velocity magnitude under the wave trough. Fig. 5(d) shows the error of the simulated velocities compared to the experimental data. The error is presented in terms of the mean absolute percentage error as: $E_r = \frac{1}{N}\sum_{n=1}^{N}\frac{|u_{n,exp}-u_{n,num}|}{|u_{n,exp}|}$ x 100, where $u_{n,num}$ is the velocity predicted, u_{exp} is the velocity measured, and N is the number of data points along the water depth at $t/T = 0.5$. It is seen that in the case of waves alone, the error ranges between E_r = 3 - 4% for ka =0.024 - 0.083 and $U_{cm} = 0$ (Test C1 - C3). However, in case of combined waves and current, the error increases to 3 - 7% for U_{cm} = 0.46 - 0.76, ka = 0.083 (Test D1 - D3).

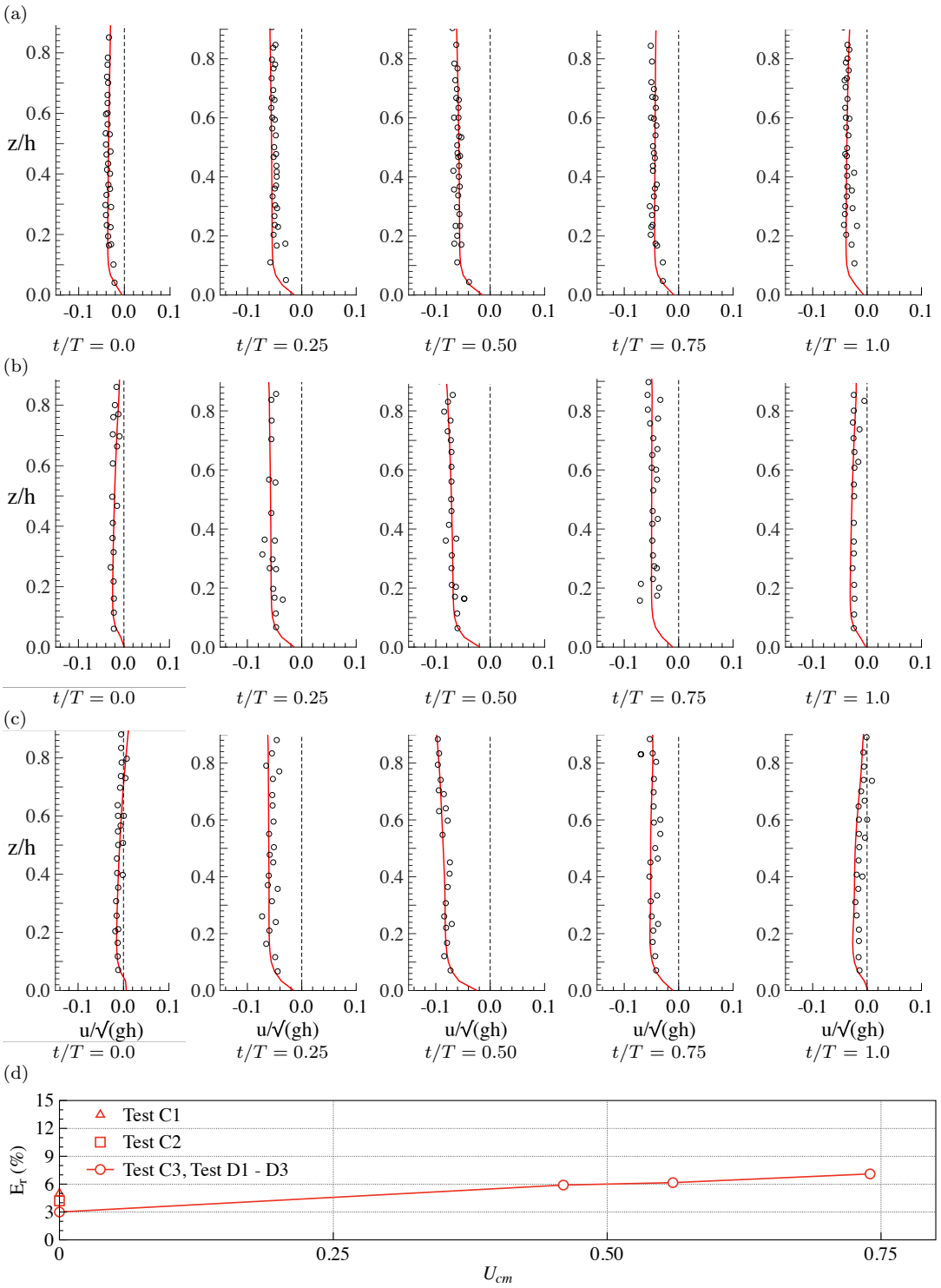

Figure 5: Simulated velocity profiles of the combined action of waves and current for different values of U_{cm} = (a) 0.74, (b) 0.56, (c) 0.46. Other test conditions: steady current velocity, $u_c/\sqrt{gh} = 0.046$, wave period T = 1.0 s, grid size dx = 0.01 m, CFL = 0.10 and the wave gauge WG1 location is x = 0 m. The red solid line: simulated result; black circles: experiment. (d) the mean absolute percentage error E_r against U_{cm} at t/T = 0.50. The red square: E_r for $ka = 0.024$, $U_{cm} = 0$ (Test C1); the red triangle: E_r for $ka = 0.054$, $U_{cm} = 0$ (Test C2); and the red circles with line: E_r for $ka = 0.083$ and $U_{cm} = 0 - 0.74$ (Test C3, Test D1 - D3); Source of the experimental data: [18].

Overall, the numerical results show that the simulated velocity profiles for the combined action of waves and current are well represented and show a satisfactory agreement with the experimental observations [18]. This confirms the validity of the model for an accurate representation of the combined action of waves and current in the NWT.

3.2. Morphological validation

This section describes the morphological validation of the model for the calculation of the scour below the pipeline with free surface. The simulations are run for pipeline scour under waves and steady current conditions. Details of the simulations performed for morphological validation are listed in Table 1.

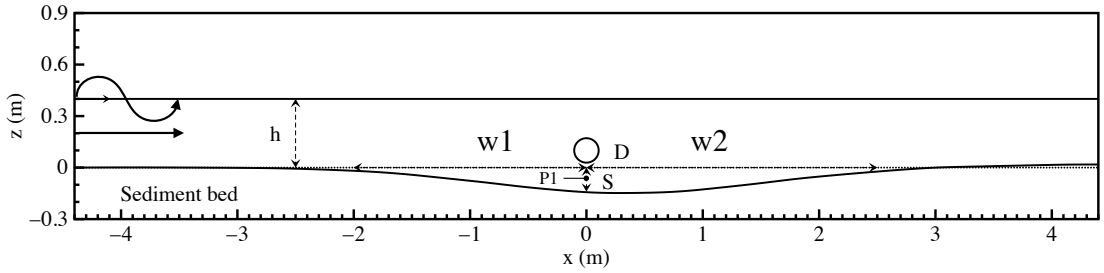

(a)

Figure 6: Numerical setup used for scour below the pipeline. The term D defines the pipeline diameter, S is maximum scour depth below the pipeline, $w = w1 + w2$ is the length of the scour hole, $w1$ and $w2$ are the horizontal extent of the scour on the upstream and the downstream side of the pipeline, respectively.

3.2.1. Pipeline scour under waves

This section describes the simulations performed to investigate scour below the pipeline under waves. The test conditions are based on the benchmark experimental investigation from Sumer and Fredsøe [3]. The NWT is the same as the one used for the hydrodynamic validation. In addition, a pipeline of diameter $D = 0.05$ m is placed at the center of the NWT as in Fig. 6(a). For the initialisation of the simulations, a negligible gap between the sediment bed and the pipeline, i.e. $e = dx/2$ is introduced for all calculations conducted for the pipeline scour. This is because the onset of the pipeline scour due to the seepage and the piping is not accounted for in the simulations. The water depth is $h = 0.40$ m, and the bottom of the NWT (z = -0.30 m) is filled with the sand. The density of the sand is 2700 kg/m^3 and the median grain size is $d_{50} = 0.58$ mm. The critical value of the Shields parameter is $\theta_c = 0.05$. The sandy bed is hydraulically rough with a roughness height $k_s = 3d_{50}$. The sediment porosity parameter is

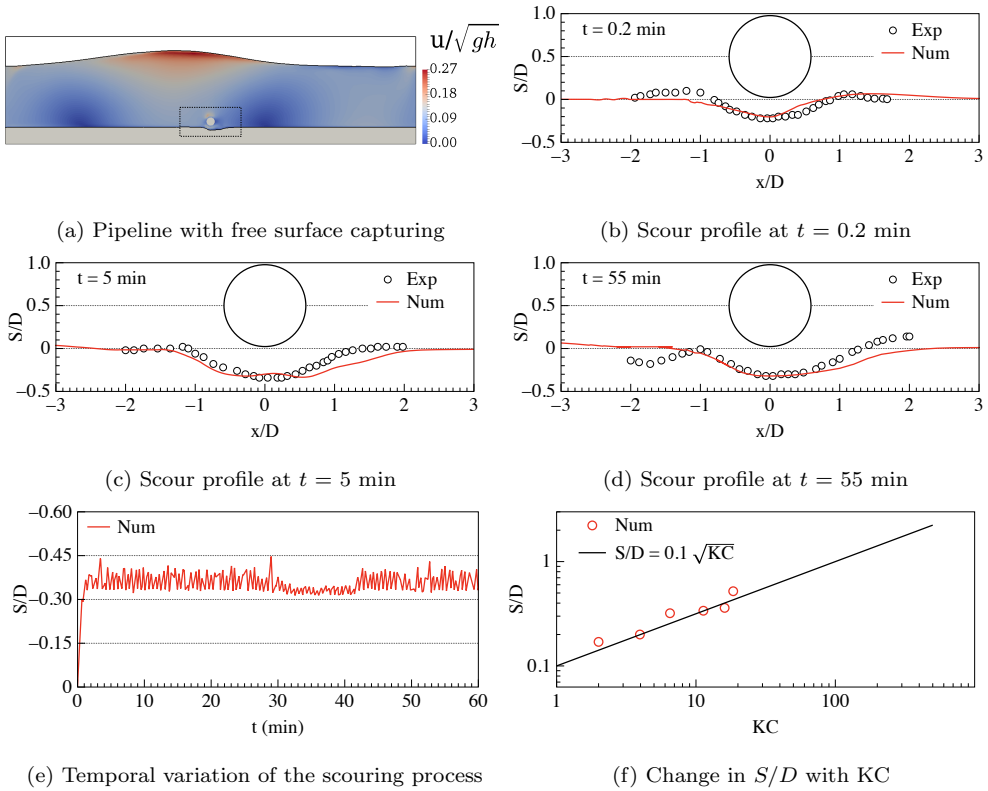

(a) Pipeline with free surface capturing

(b) Scour profile at $t = 0.2$ min

(c) Scour profile at $t = 5$ min

(d) Scour profile at $t = 55$ min

(e) Temporal variation of the scouring process

(f) Change in S/D with KC

Figure 7: Scour below the pipeline exposed to waves. Test conditions: Pipeline diameter $D = 0.05$ m, KC = 7.0. Red solid line: the numerical results; Red circles: Experimental data from Sumer and Fredsøe [3].

considered to be $n = 0.40$. For the numerical simulations, the size of the NWT is the same as the one used for the hydrodynamic validation with second-order Stokes waves as input for the wave generation. The selection of the wave theory is according to the chart for the applicability of wave theory given by Le Méhauté [51].

Fig. 7 illustrates the scour below the pipeline exposed to wave action. The numerical results provide the bed changes with the free surface, the temporal variation of the scouring process and the change of the scour depth against the KC number. Fig. 7(a) shows the pipeline scour for KC = 7.0. The interaction of the wave crest with the pipeline leads to an increase in the velocity below the pipeline and results in the onset of scour. Fig. 7(b) shows a zoomed-in view of the initial stage of scour below the pipeline at $t = 0.20$ minutes. At this stage, the scour below the pipeline is rapidly initiated with the crest action of the first wave. The scour depth is found to be $S/D = 0.25$ which is almost half of the maximum scour depth. The horizontal extent of the scour (w) below the pipeline is -1.0 $\leq w/D \leq$ +1.0. The simulated bed profile at shows a good

agreement with the experimental observations [3]. Fig. 7(c) shows the scour profile below the pipeline at $t = 5.0$ min. Here, the water jet effect in the gap between the pipeline and the bed is seen which results in tunnel scour. The maximum scour depth is seen to be $S/D = 0.45$. The horizontal extent of the scour is -1.5 $\leq w/D \leq$ +1.5. The simulated scour depth and bed profile show a satisfactory match with the experimental observations. The numerical results confirm the ability of the model to simulate the tunnel scour process, which is considered to be a crucial part of the pipeline scour as the maximum scour depth is reached during this stage [8, 14, 17]. Fig. 7(d) shows the scour profile at $t = 55$ min. This corresponds to the final stage of the scour. There is almost no change in the maximum scour depth compared to the maximum scour depth at $t = 5.0$ min. However, the horizontal extent of the scour increases to -1.5 $\leq w/D \leq$ +2.0. The horizontal extent of the scour on the downstream side of the pipeline is higher compared to the upstream side. This is due to the relatively higher influence of the lee-wakes in the wave propagation direction. The maximum scour depth below the pipeline agrees well with the experimental data. However, the length of the scour hole is slightly over-predicted. Fig. 7(e) shows the temporal variation of the scouring process for KC = 7.0. It is seen that the major part of the maximum scour takes place within the first 10 min. The maximum scour depth below the pipeline is then maintained with the scouring and refilling because of the wave crest and wave trough, respectively, as seen from the fluctuations in the curve. Fig. 7(f) shows the model performance for the calculation of the maximum scour below the pipeline for different KC numbers. The pipeline scour for KC = 7 is already discussed in detail. The results of the remaining tests show a similar scour profile with a change in the maximum scour depth and are therefore presented as the variation of the scour depth (S/D) against the KC number. It is seen that the maximum scour depth increases with the KC number. The results show a satisfactory match with the formula $S/D = 0.1\sqrt{KC}$ based on experimental observations from Sumer and Fredsøe [3].

3.2.2. Pipeline scour under a steady current

This section investigates the pipeline scour under a steady current. For this purpose, two simulations are performed based on the experiments by Mao [1]. The pipeline diameter is $D =$ 0.10 m and is placed on a sandy bed with the median particle size $d_{50} = 0.36$ mm. The still water depth is $h = 0.35$ m. For the first test, the inflow velocity is $u/\sqrt{gh} = 0.189$. The far-field Shields parameter is $\theta = 0.048$, which corresponds to a clear water scour regime. The second test is run by increasing the inflow velocity to $u/\sqrt{gh} = 0.27$. The far-field Shields parameter

for this case is $\theta = 0.09$, resulting in a live-bed scour regime.

Fig. 8(a) shows the simulated clear-water scour profile with the free surface. The maximum velocity below the pipeline is seen to be $u/\sqrt{gh} = 0.38$ which is almost two times higher than the inflow velocity. This leads to a flow jet below the pipeline and consequently larger scour. The eroded sediments are deposited on the downstream side of the pipeline. No scour is observed on the downstream side of the pipeline. This is because a scour hole with a steep bed slope leads to the flow exiting the scour below the pipeline almost vertically. This avoids the interaction of the large vortices with the horizontal bed, which are considered to be a primary cause for the scour at the downstream side of the pipeline [2]. Fig. 8(b) shows the zoomed-in view of the scour profile below the pipeline. The maximum scour is about $S/D = 0.50$. The length of the scour hole is -2.0 $\leq w/D \leq$ +3.0. The scour profile depicts a good agreement with the experimental data [1]. Fig. 8(c) shows the temporal variation of the scouring process for scour in the clear-water scour regime. The scour depth is calculated to be $S/D = 0.25$ in the beginning and attains the maximum scour depth $S/D = 0.50$ after about 30 minutes. The comparison of the numerical results with the experiments [1] shows a satisfactory agreement.

Fig. 8(d) shows the simulated live-bed scour profile with the free surface. The simulation is run by increasing the inflow velocity to $u/\sqrt{gh} = 0.27$. The maximum velocity below the pipeline is seen to be $u/\sqrt{gh} = 0.55$ which is almost two times higher compared to the velocity seen in the clear-water scour regime. The increase in the velocity below the pipeline leads to a further larger scour depth below the pipeline. Also, the horizontal extent of the scour on the downstream side of the pipeline is seen to be larger. Once the scour profile becomes less steep, the flow exits close to the horizontal bed. This allows for the interaction of the large vortices with the horizontal bed and results in larger scour at the downstream side of the pipeline. Fig. 8(e) shows a zoomed-in view of the scour profile. The maximum scour is found to be $S/D = 0.75$. The horizontal extent of the scour -3.0 $\leq w/D \leq$ +4.0. Fig. 8(f) shows the temporal variation of the scouring process in the live-bed regime. The scour depth is calculated to be $S/D = 0.50$ in the beginning which is two times higher compared to the scour depth in the clear-water regime and attains the maximum scour depth $S/D = 0.75$ within 15 minutes. The numerical results are in good agreement with the experimental observations [1].

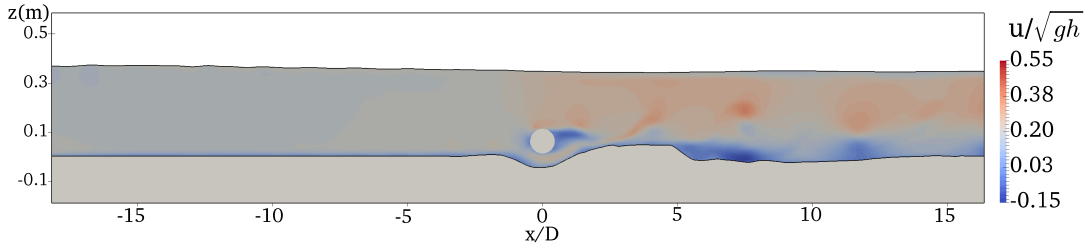

(a) Simulated scour below the pipeline for clear-water regime ($\theta < \theta_c$) with free surface

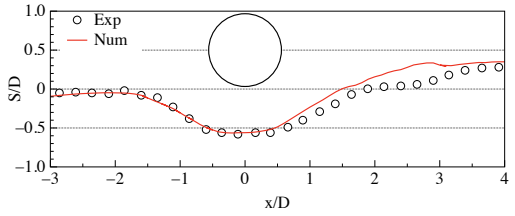

(b) Zoomed-in view, ($\theta < \theta_c$)

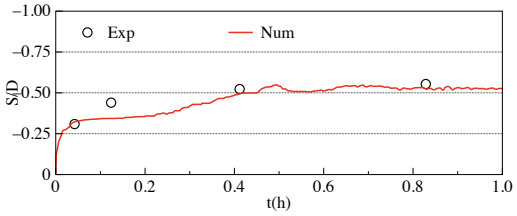

(c) Temporal variation of the process

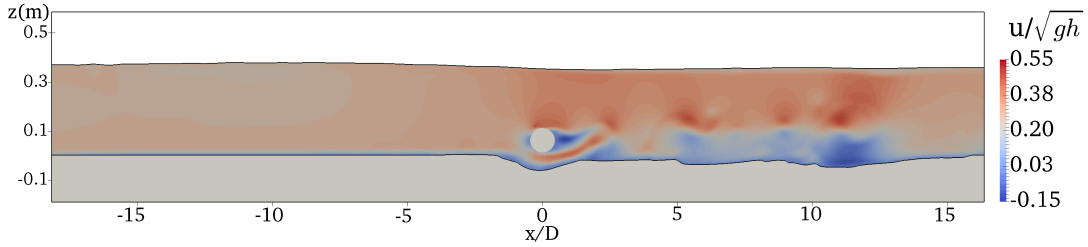

(d) Simulated scour below the pipeline for live-bed regime ($\theta > \theta_c$) with free surface

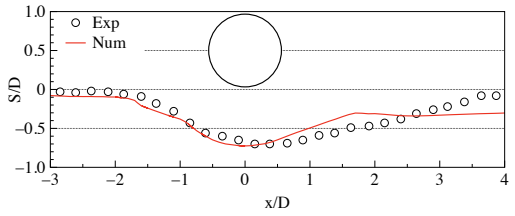

(e) Zoomed-in view, ($\theta > \theta_c$)

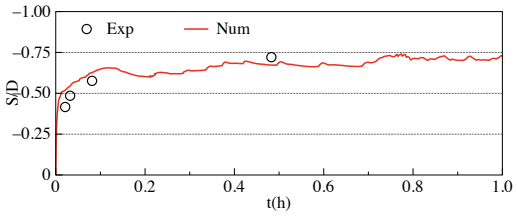

(f) Temporal variation of the process

Figure 8: The simulated pipeline scour with the free surface. (a-c) depict the scour with free surface for clear-water scour. Test conditions: inflow velocity $u/\sqrt{gh} = 0.189$ and $\theta = 0.048$ ($< \theta_c$). (d-f) depict the scour with free surface for the live-bed scour. Test conditions: Inflow velocity $u/\sqrt{gh} = 0.270$ and $\theta = 0.09$ ($> \theta_c$). The red lines are simulated results and the black circles are the experiment. Source of experimental data: Mao [1].

4. Pipeline scour under combined waves and current

In this section, the validated model is used for scour under co-directional combined waves and current. The flow conditions and sediment bed properties are based on the experimental data from Sumer and Fredsøe [8]. The pipeline diameter is $D = 0.07$ m and the still water depth

Test	$f(1/s)$	$T(s)$	$h(m)$	u_m(m/s)	$u_m/\sqrt{gh}$	$H(m)$	ka	u_c	$u_c/\sqrt{gh}$	U_{cm}	$u/\sqrt{gh}$	θ	S/D	β	$w2/w1$
KC = 5.5															
G1	0.40	2.50	0.39	0.16	0.081	0.065	0.042	0.00	0.000	0.00	0.13	0.06	0.23	0.21	1.2
G2	0.40	2.50	0.39	0.16	0.081	0.065	0.042	0.09	0.044	0.35	0.17	0.10	0.28	0.30	1.7
G3	0.40	2.50	0.39	0.16	0.081	0.065	0.042	0.15	0.077	0.49	0.23	0.20	0.47	0.75	2.2
G4	0.40	2.50	0.39	0.16	0.081	0.065	0.042	0.26	0.131	0.62	0.32	0.20	0.75	1.12	3.0
KC = 10															
H1	0.32	3.13	0.39	0.23	0.118	0.082	0.037	0.00	0.000	0.00	0.22	0.10	0.42	0.45	1.5
H2	0.32	3.13	0.39	0.23	0.118	0.082	0.037	0.13	0.064	0.35	0.30	0.20	0.46	0.70	2.1
H3	0.32	3.13	0.39	0.23	0.118	0.082	0.037	0.21	0.108	0.49	0.39	0.30	0.55	0.90	2.5
H4	0.32	3.13	0.39	0.23	0.118	0.082	0.037	0.37	0.190	0.62	0.48	0.40	0.77	1.20	3.0
KC = 18															
I1	0.22	4.55	0.39	0.27	0.138	0.108	0.037	0.00	0.000	0.00	0.40	0.10	0.45	0.57	1.6
I2	0.22	4.55	0.39	0.27	0.138	0.108	0.037	0.14	0.072	0.34	0.45	0.20	0.55	0.77	2.3
I3	0.22	4.55	0.39	0.27	0.138	0.108	0.037	0.24	0.123	0.47	0.47	0.25	0.62	0.91	2.8
I4	-	-	0.39	-	-	-	-	0.37	0.190	1.00	0.32	0.20	0.80	0.91	3.1

Table 2: List of the simulations performed for the pipeline scour under the co-directional combined waves and current. The flow is generated from left-to-right. Experimental data: Sumer and Fredsøe [8].

is $h = 0.39$ m. The bed material consists of sand with $d_{50} = 0.16$ mm. Three sets of simulations are run for different values of U_{cm} corresponding to KC = 5.5, 10, 18 with U_{cm} varying between 0 and 1.0. The conditions of the simulations are summarised in Table 2.

4.1. Scour for different values of U_{cm}, KC = 5.5

Fig. 9 shows the scour below the pipeline with the free surface for the combined waves and current. The incident wave conditions are kept constant (KC = 5.5) and the different values of U_{cm} are obtained by increasing the steady current velocity. Fig. 9(a) shows the maximum scour below the pipeline for $U_{cm} = 0$, corresponding to waves alone. The maximum velocity below the pipeline during the wave crest is seen to be $u/\sqrt{gh} = 0.13$ (see Table 2). The scour depth below the pipeline is seen to be $S/D = 0.23$. The horizontal extent of the scour on the upstream and the downstream side (β) is found to be almost symmetrical.

Fig. 9(b) shows the scour below the pipeline for $U_{cm} = 0.35$. This case corresponds to a steady current with the velocity $u_c/\sqrt{gh} = 0.044$ combined with waves of KC = 5.5. The velocity below the pipeline during the incidence of the wave crest is seen to be $u/\sqrt{gh} = 0.17$. The maximum scour below the pipeline is $S/D = 0.28$. The scour is relatively deeper compared to the waves alone condition. This is due to an increase in the velocity below the pipeline when a steady current is combined with waves. In addition, the current represents an additional transport mechanism for the sediment particles already in bed and suspended load in the vicinity

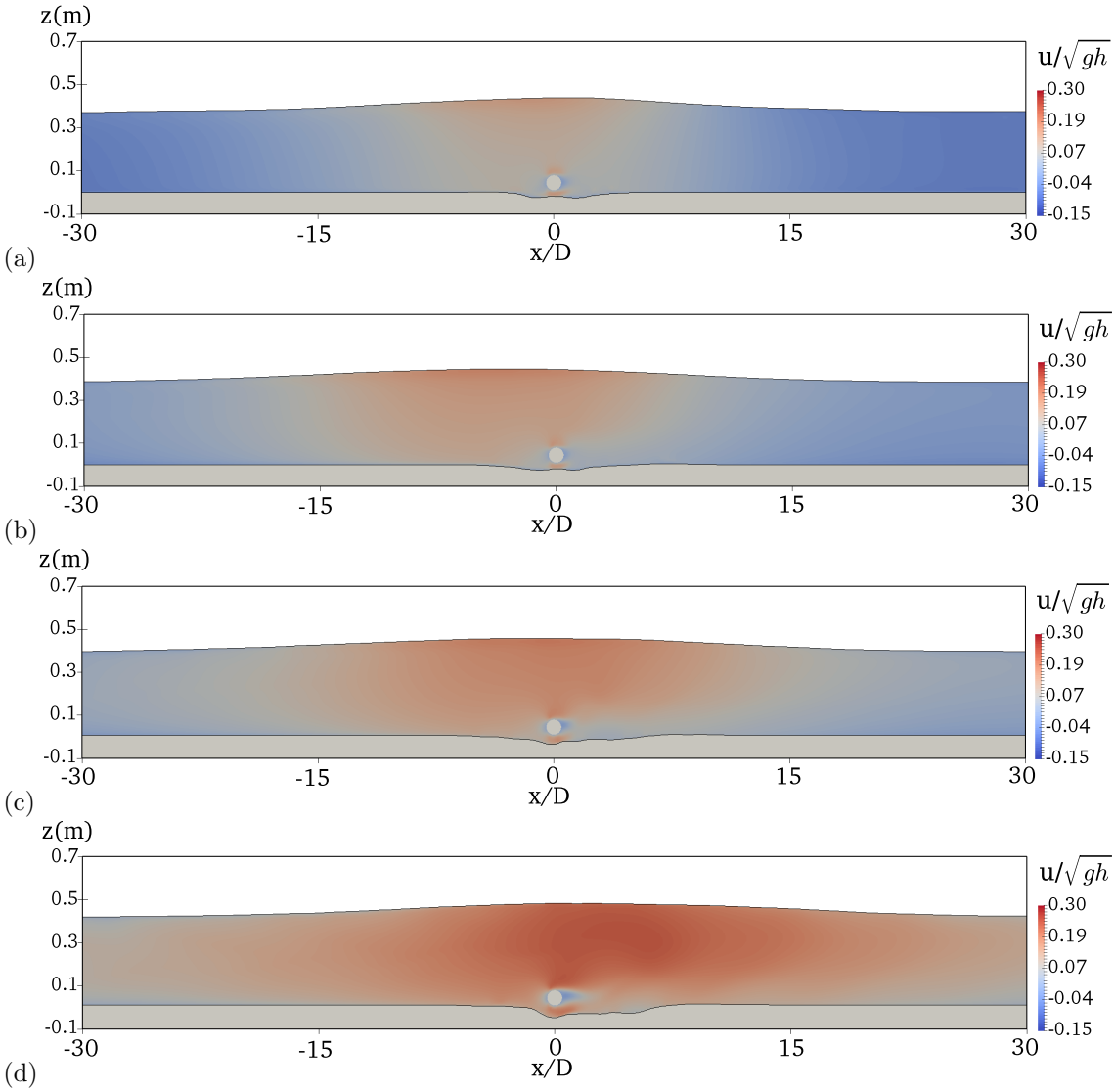

Figure 9: Simulated scour profiles with free surface for different values of U_{cm}, KC = 5.5. (a) $U_{cm} = 0$, (b) $U_{cm} = 0.35$, (c) $U_{cm} = 0.49$, (d) $U_{cm} = 0.62$.

of the pipeline. The result is an asymmetric scour geometry, extending further in the direction of the steady current. Fig. 9(c) shows pipeline scour for $U_{cm} = 0.49$. This case corresponds to the condition when the steady current velocity is increased to $u_c/\sqrt{gh} = 0.077$. The scour below the pipeline is found to be $S/D = 0.47$, which is almost two times the scour under waves alone, and the horizontal extent of the scour is larger in wave direction. The simulated result agrees with the previous explanation that the presence of the steady current leads to a larger sediment mobilisation in the wave direction. Fig. 9(d) shows pipeline scour with free surface

profile for $U_{cm} = 0.62$, when the steady current velocity is increased to $u_c/\sqrt{gh} = 0.131$. The maximum scour depth below the pipeline increases to $S/D = 0.75$, which is almost three times larger than the scour under waves alone.

A correlation between the velocities and resulting scour below the pipeline with U_{cm} is evident in Fig. 10. The numerical analysis examines the simulated scour against the experimental observations from [8]. The term $u/\sqrt{gh}$ is the maximum velocity measured below the pipeline and S/D is the corresponding maximum scour depth. The term β is defined as an increase

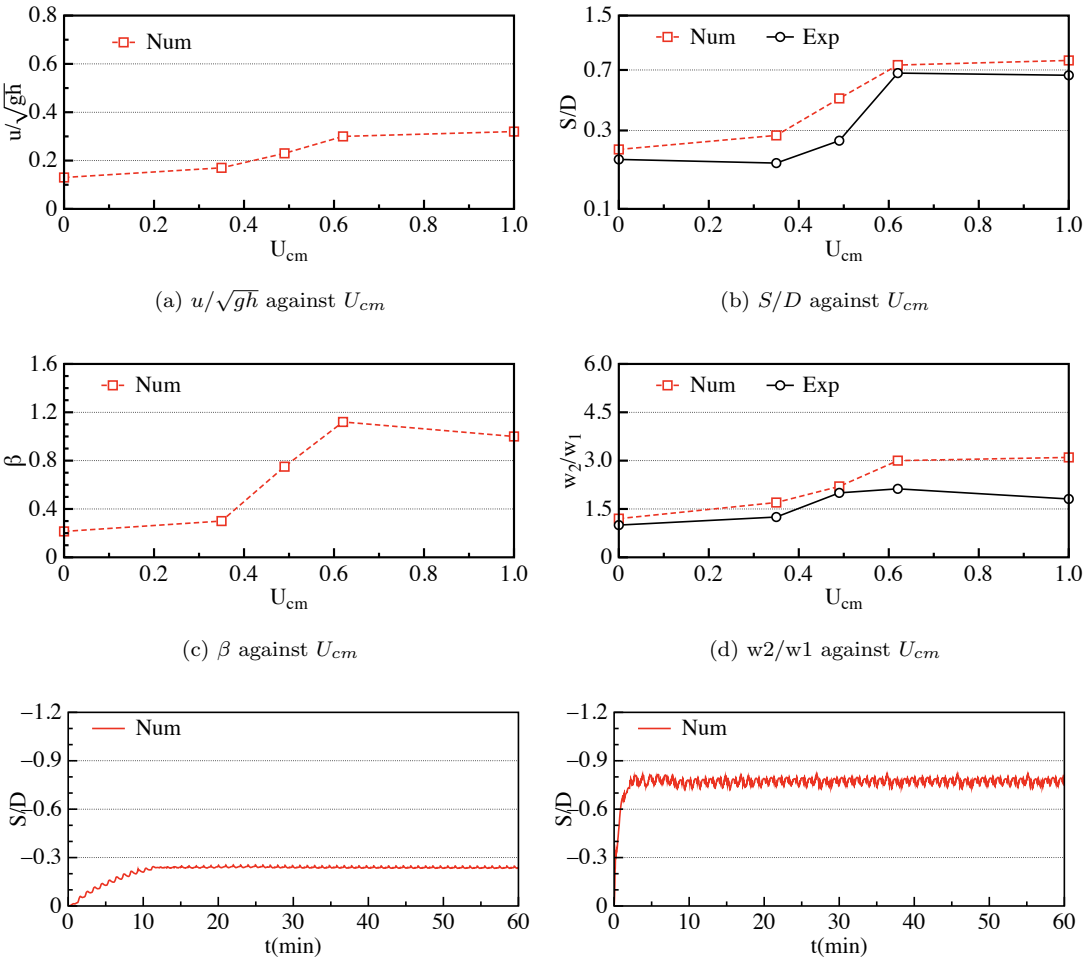

(a) $u/\sqrt{gh}$ against U_{cm}

(b) S/D against U_{cm}

(c) β against U_{cm}

(d) w2/w1 against U_{cm}

(e) Temporal variation of S/D, $U_{cm} = 0$

(f) Temporal variation of S/D, $U_{cm} = 0.62$

Figure 10: The velocity and resulting scour below the pipeline corresponding to an increasing U_{cm}, KC = 5.5. The term $U_{cm} = 0$ represents waves alone and $u_{wc} = 0$ means current alone. The velocity below the pipeline is measured at point $P1$ $x/D = 0$, z/D = -0.10 (see Fig. 6(a)).

in the velocity under the wave crest ($u_{m,cr}$) compared to that under the wave trough ($u_{m,tr}$) as $\beta = (u_{m,cr} - u_{m,tr})/u_{m,cr}$ and $w2/w1$ is the relative scour extent, where $w1$ and $w2$ are the horizontal extent of the scour on the upstream and the downstream side of the pipeline, respectively. Figs. 10(a-b) show $u/\sqrt{gh}$ and S/D versus U_{cm} for KC = 5.5, respectively. It appears that $u/\sqrt{gh}$ increases from 0.13 to 0.32 and S/D increases from 0.23 to 0.75 for U_{cm} in the range 0 to 0.62 (see also Table 2, test (G1-G4)).

Figs. 10(c-d) show β and $w2/w1$ versus U_{cm}, respectively. As β increases from 0.21 to 1.12, $w2/w1$ increases from 1.2 to 3.0, signifying a larger horizontal extent of the scour in the wave direction as the steady current velocity increases. Figs. 10(e-f) show the temporal evolution of the scour (S/D versus time) for $U_{cm} = 0$ and 0.62. The results for $U_{cm} = 0.35$ and 0.49, show a similar pattern of S/D versus time with a change in the magnitude and are therefore presented as the change in scour depth (S/D) against U_{cm} as in Fig. 10(b). For $U_{cm} = 0$ the equilibrium scour depth is $S/D = 0.23$ and is attained within 10 minutes (Fig. 10(e)). For $U_{cm} = 0.62$ it is seen that the initial scour development is rapid; the equilibrium scour depth is $S/D = 0.75$ and is attained within 5 minutes.

4.2. Scour for different values of U_{cm}, KC = 10

Figs. 11(a-d) show S/D for $U_{cm} = 0$, 0.35, 0.49, 0.62 and the maximum scour depth below the pipeline is seen to be $S/D = 0.42$, 0.46, 0.55, 0.77, respectively. The simulated maximum scour depth S/D and the horizontal extent of the scour for $U_{cm} = 0$ are larger than for KC = 5.5, but follow the same pattern. As before, an increase in U_{cm} results in an increase in S/D and a larger horizontal extent on the downstream side of the pipeline.

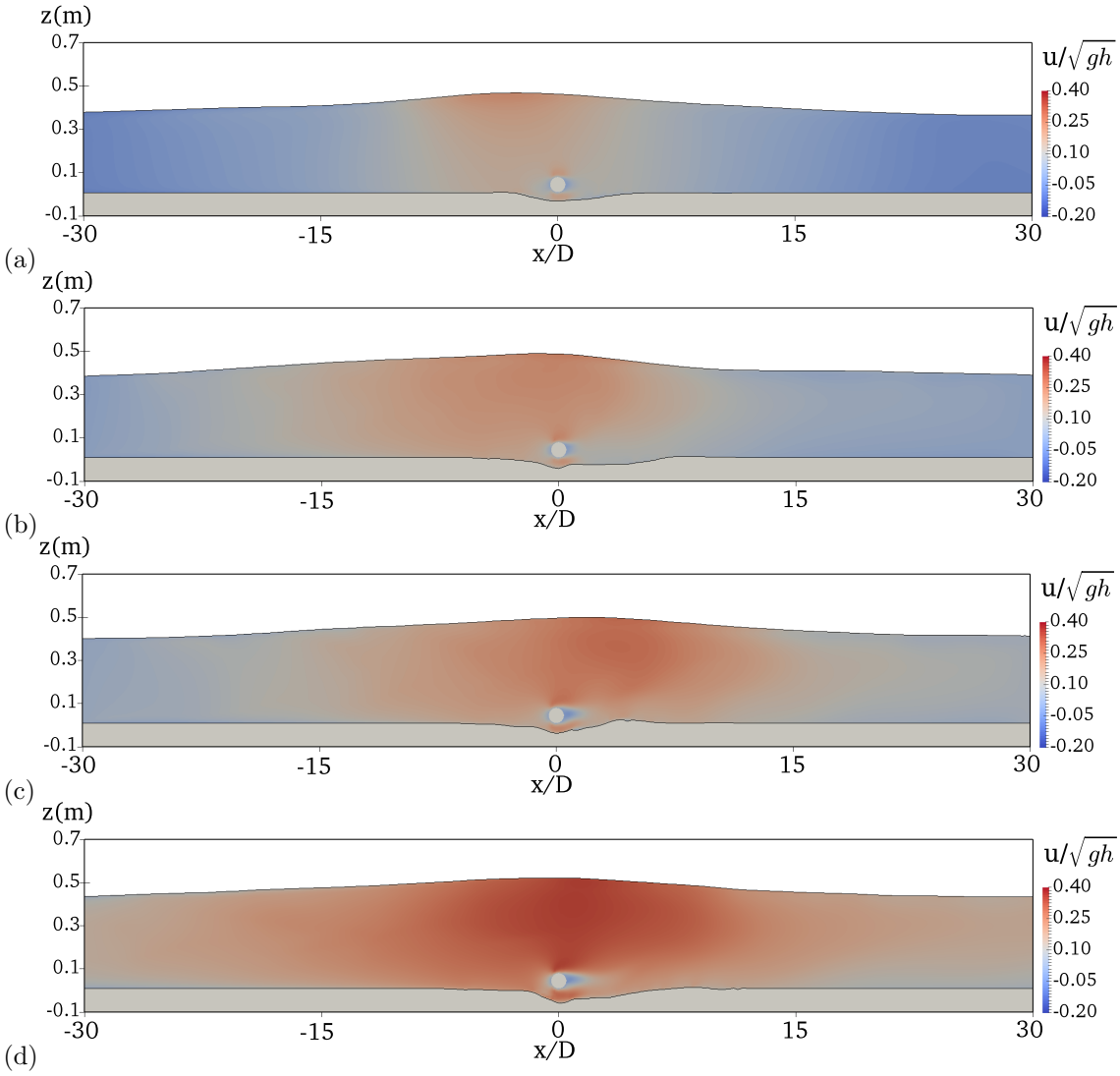

Figure 11: Simulated scour profiles with free surface for different values of U_{cm}, KC = 10. (a) $U_{cm} = 0$, (b) $U_{cm} = 0.35$, (c) $U_{cm} = 0.49$, (d) $U_{cm} = 0.62$.

Figs. 12(a-b) present $u/\sqrt{gh}$ and S/D against U_{cm}, respectively, for KC = 10. It is seen that $u/\sqrt{gh}$ increases from 0.22 to 0.48 and S/D varies from 0.42 to 0.77, following the trend measured in the experiment. At the same time, the curve in Fig. 12(b) is flatter than in Fig. 10 (b), where the difference between currents alone and waves alone is higher. Figs. 12(c-d) show the variation for β and $w2/w1$; also here the curves are flatter than observed for KC = 5.5. This behavior, following the tendency of S/D in Fig. 12(b), is attributed to that the higher KC number leads to higher scour than for $U_{cm} = 0$. Figs. 12(e-f) show the temporal evolution

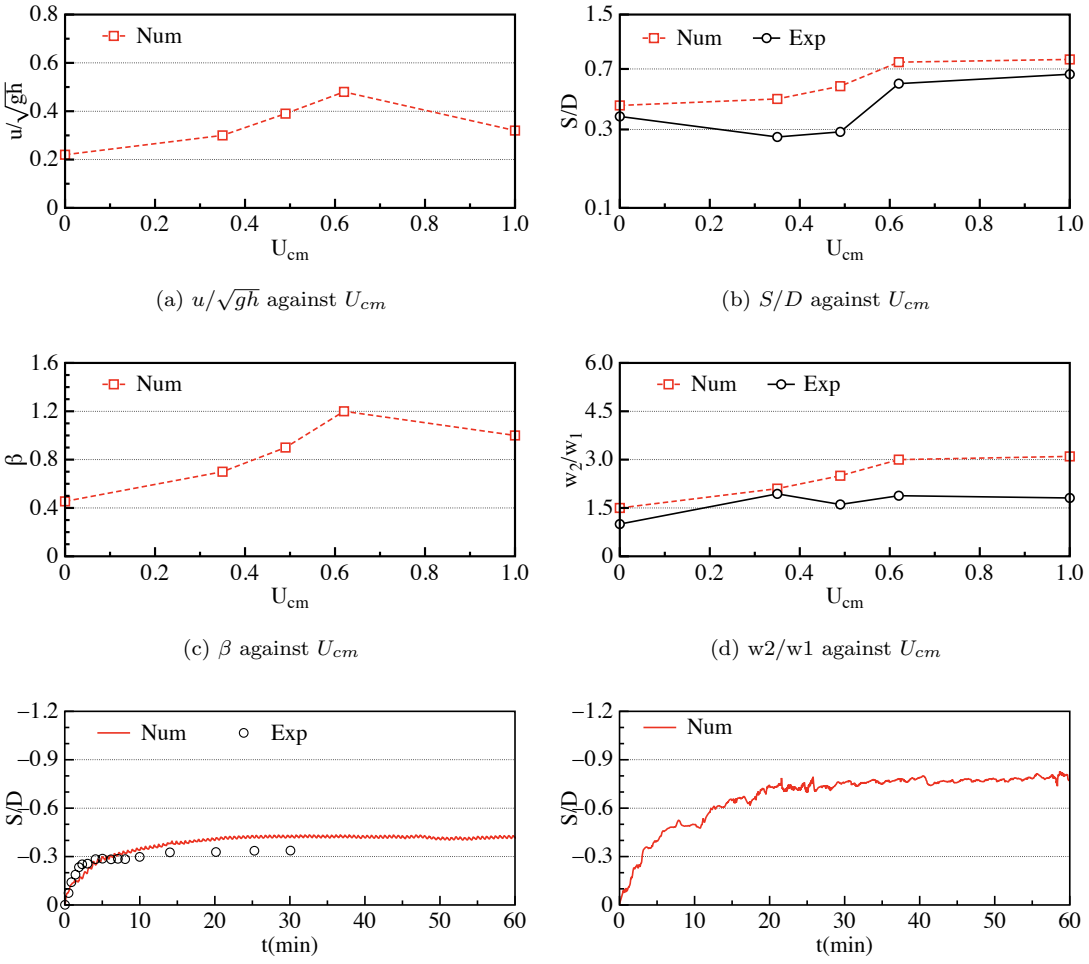

(a) $u/\sqrt{gh}$ against U_{cm}

(b) S/D against U_{cm}

(c) β against U_{cm}

(d) w2/w1 against U_{cm}

(e) Temporal variation of S/D, $U_{cm} = 0$

(f) Temporal variation of S/D, $U_{cm} = 0.62$

Figure 12: Variation in the velocity and resulting scour below the pipeline corresponding to an increasing U_{cm}, KC = 10

of S/D for $U_{cm} = 0$ and 0.62, respectively. The simulated temporal variation of the process is in good agreement with the experimental observation [8] for $U_{cm} = 0$ (waves alone).

4.3. Scour for different values of U_{cm}, KC = 18

In order to further investigate the effect of combined waves and current on the scour development, four simulations are run for $U_{cm} = 0$, 0.34, 0.47 and 1.0 for KC = 18. Figs. 13(a-c) show the scour profile for $U_{cm} = 0$, 0.34 and 0.47 and the maximum scour depth below the pipeline is seen to be $S/D = 0.45$, 0.55 and 0.62, respectively. Fig. 13(d) shows the pipeline scour for $U_{cm} = 1.0$, corresponding to scour for current alone. The maximum scour below the

pipeline is $S/D = 0.80$. Figs. 14(a-d), showing the variation of $u/\sqrt{gh}$ and S/D, depicts a similar pattern as observed for increasing KC numbers in combination with a current: The flow intensity and scour magnitude are overall increased, while showing a lesser difference between $U_{cm} = 0$ (waves alone) and $U_{cm} = 0.62$. Overall, some small differences in the numerical results for S/D are observed, while closely following the overall trend for increasing U_{cm}. The temporal variation of the maximum scour for $U_{cm} = 0$ and 1.0 are given in Figs. 14(e-f), showing fairly good agreement with the experimental data [8] for the waves alone situation.

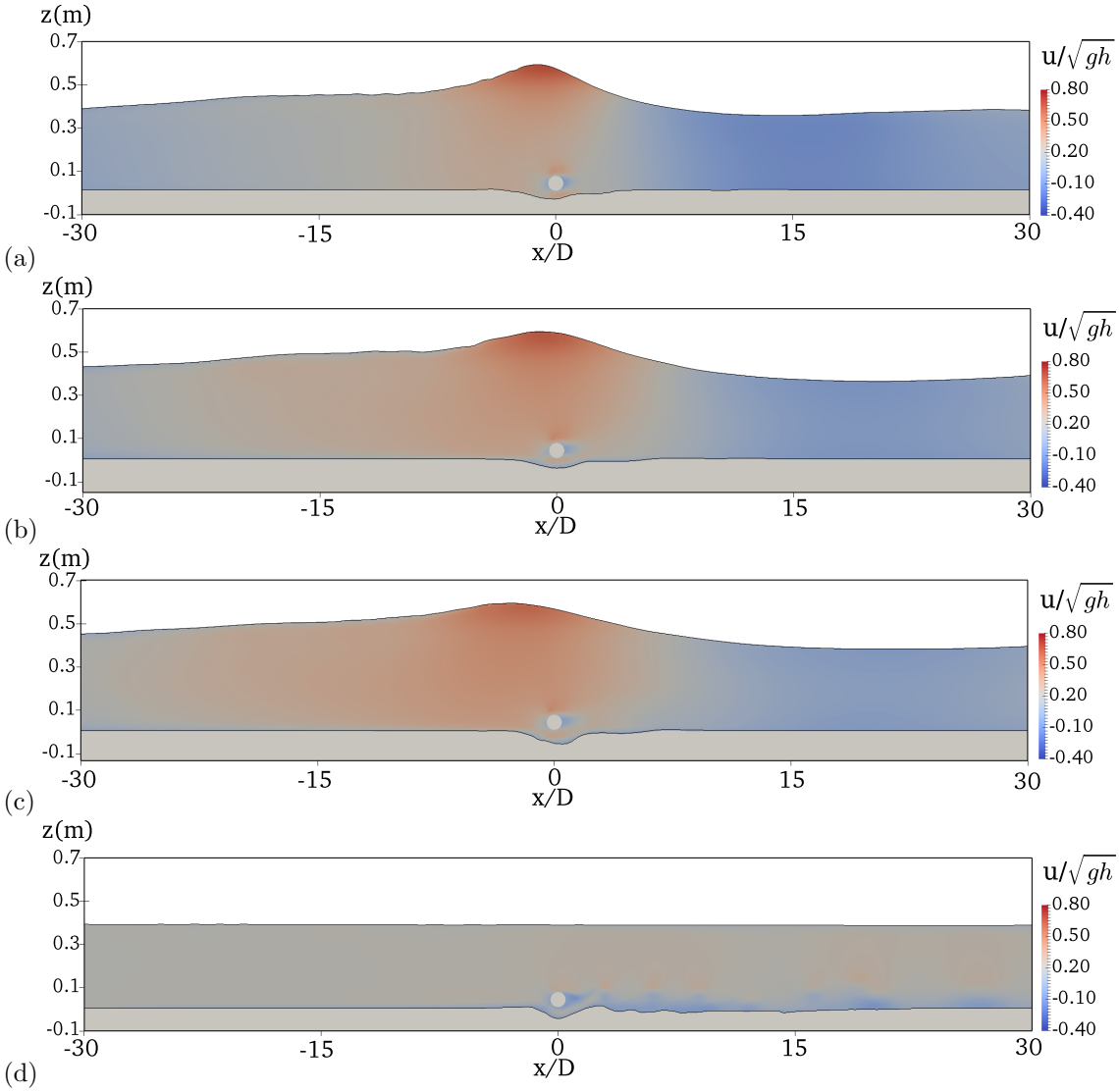

Figure 13: Simulated scour profiles with free surface for different values of U_{cm}, KC = 18. (a) $U_{cm} = 0$, (b) $U_{cm} = 0.34$, (c) $U_{cm} = 0.47$, (d) $U_{cm} = 1.0$.

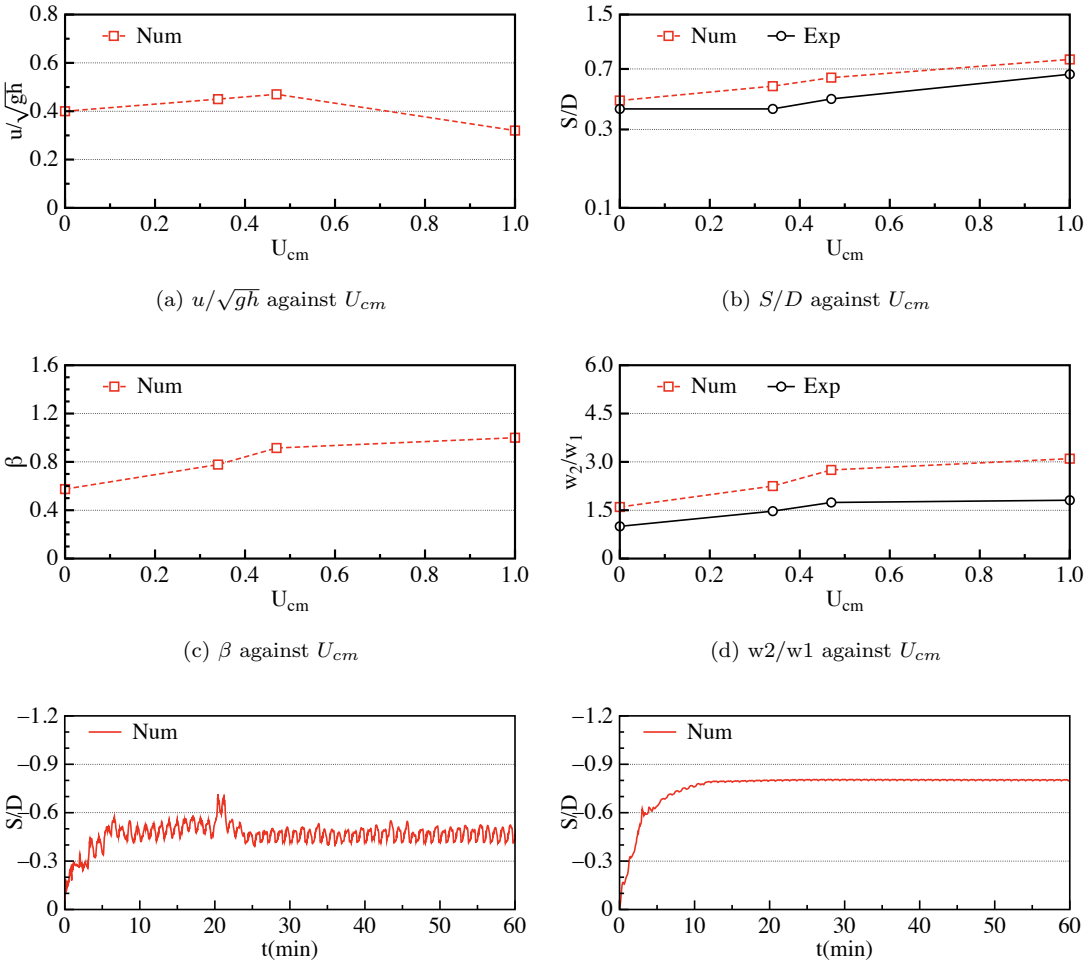

(a) $u/\sqrt{gh}$ against U_{cm}

(b) S/D against U_{cm}

(c) β against U_{cm}

(d) w2/w1 against U_{cm}

(e) Temporal variation of S/D, $U_{cm} = 0$

(f) Temporal variation of the scour depth, $U_{cm} = 0.62$

Figure 14: Variation in the velocity and resulting scour below the pipeline corresponding to an increasing U_{cm}, KC = 18. The wave gauge location is $x/D = 0$, z/D = -0.30

5. Summary and conclusions

This paper presents numerical modelling of pipeline scour under combined waves and current including the free surface. The open-source CFD model REEF3D is used to simulate the flow hydrodynamics by solving the RANS equations with the k-ω turbulence model and a sediment transport model. The RANS-equations are discretised with a finite difference method on a staggered grid. The dynamic free surface is captured with the level set method. The simulated wave hydrodynamics are coupled with sediment transport algorithms. The modified critical bed shear stress is accounted for by calculating the critical bed shear stress on the sloping bed. In

order to obtain a realistic representation of the scour hole geometry below the pipeline, a sand-slide algorithm is incorporated to correct the bed slope when it exceeds the angle of repose φ. The calculation of the bed changes is performed with the Exner equation, based on the sediment continuity at the bed.

First, a thorough hydrodynamic validation is performed by using second-order Stokes waves in numerical wave tank without the presence of the pipeline. The quality of the waves is tested through grid and time step convergence studies. The model is applied to simulate flow under co-directional combined action of second-order Stokes waves and current. Further, a series of simulations are performed for different values of the non-dimensional parameter for combined waves and current U_{cm}. The velocity profiles are compared with the experimental data from [18] and a satisfactory agreement is found. A series of simulations are run to investigate the scour below the pipeline under waves for different KC numbers. The maximum scour depth below the pipeline is found to increase with the KC number, which confirms the experimental observations from Sumer and Fredsøe [3]. Simulations are also performed to validate the pipeline scour under steady current for clear-water and live-bed conditions. The scour profile and the temporal variation of the scouring process correlate fairly well with the Mao [1] experimental results.

The validated model is used to investigate pipeline scour under combined waves and current while resolving the dynamic free surface motion. A series of simulations are run for different values U_{cm} for KC = 5.5, 10 and 18. The wave hydrodynamics, the scour profiles below the pipeline and the temporal variation of the scour process are successfully simulated. It is found that the scour depth and the horizontal extent of the scour hole below the pipeline increase with U_{cm} for a given KC number. At the same time, the relative difference in scour depth between $U_{cm} = 0$ (waves alone) and $U_{cm} = 1.0$ (current alone) is reduced, as the KC number is increased. Overall, the numerical model satisfactorily predicts pipeline scour under the combined waves and current when compared with the experimental data by Sumer and Fredsøe [8]. The present study represents an advance in the numerical scour modelling by including the dynamic free surface and the ability to account for the combined effects of waves and current.

Acknowledgements

Funding supports this research work is received from The Polish-Norwegian Research Programme operated by the National Centre for Research and Development under the Norwegian Financial Mechanism 2009-2014 under the Project No. POL-NOR/200336/95/2014. This study

was supported in part with computational resources at the Norwegian University of Science and Technology provided by NOTUR (NN2620K), http://www.notur.no.

References

[1] Y. Mao, The interaction between a pipeline and an erodible bed, PhD thesis, Technical University of Denmark, Lyngby, Denmark., 1986.

[2] B. Sumer, H. Jensen, Y. Mao, J. Fredsøe, Effect of Lee-Wake on Scour Below Pipelines in Current, Journal of Waterway, Port, Coastal, and Ocean Engineering 114 (5) (1998) 599–614.

[3] B. M. Sumer, J. Fredsøe, Scour below Pipelines in Waves, Journal of Waterway, Port, Coastal, and Ocean Engineering 116 (3) (1990) 307–323.

[4] J. Westerhorstmann, J. Machemehl, C. Jo, Effect of pipe spacing on marine pipeline scour, in: The Second International Offshore and Polar Engineering Conference, International Society of Offshore and Polar Engineers, 1992.

[5] R. J. S. Whitehouse, Scour at marine structures: A manual for practical applications, Thomas Telford, 1998.

[6] Y. Wu, Y. Chiew, Mechanics of Three-Dimensional Pipeline Scour in Unidirectional Steady Current, Journal of Pipeline Systems Engineering and Practice 4 (1) (2013) 3–10.

[7] R. Lucassen, Scour underneath submarine pipelines, Publisher: TU Delft, Civil Engineering and Geosciences, Hydraulic Engineering, 1984.

[8] B. M. Sumer, J. Fredsøe, Scour around pipelines in combined waves and current, Tech. Rep., American Society of Mechanical Engineers, New York, NY (United States), 1996.

[9] D. Myrhaug, M. C. Ong, H. Føien, C. Gjengedal, B. J. Leira, Scour below pipelines and around vertical piles due to second-order random waves plus a current, Ocean Engineering 36 (8) (2009) 605–616.

[10] B. Brørs, Numerical Modeling of Flow and Scour at Pipelines, Journal of Hydraulic Engineering 125 (5) (1999) 511–523.

[11] F. Li, L. Cheng, Prediction of lee-wake scouring of pipelines in currents, Journal of waterway, port, coastal, and ocean engineering 127 (2) (2001) 106–112.

[12] D. Liang, L. Cheng, F. Li, Numerical modeling of flow and scour below a pipeline in currents: Part II. Scour simulation, Coastal engineering 52 (1) (2005) 43–62.

[13] D. Liang, L. Cheng, Numerical model for wave-induced scour below a submarine pipeline, Journal of waterway, port, coastal, and ocean engineering 131 (5) (2005) 193–202.

[14] D. Fuhrman, C. Baykal, B. Sumer, N. Jacobsen, J. Fredsøe, Numerical simulation of wave-induced scour and backfilling processes beneath submarine pipelines, Coastal Engineering 94 (2014) 10 – 22, ISSN 0378-3839.

[15] M. Liu, L. Lu, B. Teng, M. Zhao, G. Tang, Numerical modeling of local scour and forces for submarine pipeline under surface waves, Coastal Engineering 116 (2016) 275 – 288, ISSN 0378-3839.

[16] E. Hansen, Scour Below Pipelines and Cables, A Simple Model, in: Proceedings of the International Conference on Offshore Mechanics and Arctic Engineering, American Society of Mechanical Engineers, 133–133, 1992.

[17] B. Larsen, D. Fuhrman, B. Sumer, Simulation of wave-plus-current scour beneath submarine pipelines, Journal of Waterway, Port, Coastal, and Ocean Engineering 142 (5) (2016) 04016003.

[18] M. Umeyama, Coupled PIV and PTV Measurements of Particle Velocities and Trajectories for Surface Waves Following a Steady Current, Journal of Waterway, Port, Coastal, and Ocean Engineering 137 (2) (2011) 85–94.

[19] H. Bihs, A. Kamath, M. Alagan Chella, A. Aggarwal, Ø. A. Arntsen, A new level set numerical wave tank with improved density interpolation for complex wave hydrodynamics, Computers & Fluids 140 (2016) 191–208.

[20] H. Bihs, A. Kamath, A combined level set/ghost cell immersed boundary representation for floating body simulations, International Journal for Numerical Methods in Fluids 83 (12) (2017) 905–916.

[21] A. Kamath, H. Bihs, M. Alagan Chella, Ø. A. Arntsen, Upstream-Cylinder and Downstream-Cylinder Influence on the Hydrodynamics of a Four-Cylinder Group, J. Waterw. Port Coast. Ocean Eng. DOI: 10.1061/(ASCE)WW.1943-5460.0000339.

[22] M. C. Ong, A. Kamath, H. Bihs, M. S. Afzal, Numerical simulation of free-surface waves past two semisubmerged horizontal circular cylinders in tandem, Marine Structures 52 (2017) 1–14.

[23] H. Bihs, M. Alagan Chella, A. Kamath, Ø. A. Arntsen, Numerical Investigation of Focused Waves and Their Interaction With a Vertical Cylinder Using REEF3D, Journal of Offshore Mechanics and Arctic Engineering 139 (4) (2017) 041101.

[24] M. S. Afzal, H. Bihs, A. Kamath, Ø. A. Arntsen, Three-Dimensional Numerical Modeling of Pier Scour Under Current and Waves Using Level-Set Method, Journal of Offshore Mechanics and Arctic Engineering 137 (3) (2015) 032001.

[25] N. Ahmad, H. Bihs, D. Myrhaug, A. Kamath, Ø. A. Arntsen, Three-dimensional numerical modelling of wave-induced scour around piles in a side-by-side arrangement, Coastal Engineering 138 (2018) 132 – 151.

[26] N. Ahmad, H. Bihs, M. Alagan Chella, Ø. A. Arntsen, CFD Modelling of Arctic Coastal Erosion due to Breaking Waves, International Journal of Offshore and Polar Engineering 28 (2018).

[27] D. C. Wilcox, Turbulence modeling for CFD, DCW Industries Inc., La Canada, California., 1994.

[28] D. Naot, W. Rodi, Calculation of secondary currents in channel flow, Journal of the Hydraulics Division 108 (8) (1982) 948–968.

[29] N. G. Jacobsen, D. R. Fuhrman, J. Fredsøe, A wave generation toolbox for the open-source CFD library: OpenFOAM, International Journal for Numerical Methods in Fluids 70 (9) (2012) 1073–1088.

[30] B. E. Larsen, D. R. Fuhrman, On the over-production of turbulence beneath surface waves in Reynolds-averaged Navier–Stokes models, Journal of Fluid Mechanics 853 (2018) 419–460.

[31] M. S. Hossain, W. Rodi, Mathematical modelling of vertical mixing in stratified channel flow, in: Proc. 2nd Int. Symp. on Stratified Flows, Trondheim, Norway, 1980, 1980.

[32] G. S. Jiang, C. W. Shu, Efficient implementation of weighted ENO schemes, Journal of Computational Physics 126 (1996) 202–228.

[33] M. Griebel, T. Dornseifer, T. Neunhoeffer, Numerical simulation in fluid dynamics: a practical introduction, SIAM, 1998.

[34] A. Chorin, Numerical solution of the Navier-Stokes equations, Mathematics of Computation 22 (1968) 745–762.

[35] H. van der Vorst, Bi-CGSTAB: A fast and smoothly converging variant of Bi-CG for the solution of nonsymmetric linear systems, SIAM Journal on scientific and Statistical Computing 13 (1992) 631–644.

[36] S. F. Ashby, R. D. Falgout, A parallel multigrid preconditioned conjugate gradient algorithm for groundwater flow simulations, Nuclear Science and Engineering 124 (1) (1996) 145–159.

[37] S. Osher, J. A. Sethian, Fronts propagating with curvature-dependent speed: algorithms based on Hamilton-Jacobi formulations, Journal of Computational Physics 79 (1988) 12–49.

[38] G. S. Jiang, D. Peng, Weighted ENO schemes for Hamilton-Jacobi equations, SIAM Journal on Scientific Computing 21 (2000) 2126–2143.

[39] C. W. Shu, S. Osher, Efficient implementation of essentially non-oscillatory shock capturing schemes, Journal of Computational Physics 77 (1988) 439–471.

[40] D. Peng, B. Merriman, S. Osher, H. Zhao, M. Kang, A PDE-based fast local level set method, Journal of Computational Physics 155 (1999) 410–438.

[41] L. C. van Rijn, Sediment Transport, Part I: Bed Load Transport, Journal of Hydraulic Engineering 110 (10) (1984) 1431–1456.

[42] S. Dey, Threshold of sediment motion on combined transverse and longitudinal sloping beds, Journal of Hydraulic Research 41 (4) (2003) 405–415.

[43] A. Roulund, B. M. Sumer, J. Fredsøe, J. Michelsen, Numerical and experimental investigation of flow and scour around a circular pier, Journal of Fluid Mechanics 534 (2005) 351–401.

[44] M. G. M. Burkow, A full three-dimensional numerical simulation of sediment transport and the scouring at a rectangular obstacle, Computers and Fluids 125 (2016) 1–10.

[45] B. M. Sumer, A. Roulund, J. Fredsøe, J. Michelsen, Three-dimensional numerical modeling of flow and scour around a pile, in: Proc., 1*st* International Conference on scour of foundations, 795–809, 2002.

[46] D. Lysne, Movement of Sand in Tunnels, River and Harbour Laboratory at The Technical University of Norway, River and Harbour Laboratory at The Technical University of Norway, 1970.

[47] W. Wu, W. Rodi, T. Wenka, 3D Numerical Modeling of Flow and Sediment Transport in Open Channels, Journal of Hydraulic Engineering 126 (1) (2000) 4–15.

[48] R. G. Dean, R. A. Dalrymple, Water wave mechanics for engineers and scientists, World Scientific, 1991.

[49] P. Higuera, L. J. Lara, I. J. Losada, Realistic wave generation and active wave absorption for Navier Stokes models Application to OpenFOAM, Coast. Eng. 71 (2013) 102–118.

[50] P. A. Berthelsen, O. M. Faltinsen, A local directional ghost cell approach for incompressible viscous flow problems with irregular boundaries, Journal of Computational Physics 227 (2008) 4354–4397.

[51] B. L. Méhauté, An introduction to hydrodynamics and water waves, Springer-Verlag, New York, 1976.

6. Notations

The following symbols are used in this paper:

β = transverse bed slope;

φ = angle of repose;

η = ratio of the drag force to the inertia force;

τ = bed shear stress;

τ_0 = Shields critical bed shear stress on horizontal bed;

τ_{cr} = modified critical bed stress;

$\widetilde{\tau}$ = critical bed shear stress ratio;

ρ = fluid density;

ρ_s = sediment density;

ν = fluid kinematic viscosity;

ν_t = eddy viscosity;

ω = specific turbulent dissipation;

$\phi(\vec{x}, t)$ = level set function;

κ = von Karman constant;

$q_{b,i}$ = bed-load transport rate;

Γ = sediment mixing coefficient;

θ = Shields parameter;

θ_c = critical Shields parameter;

λ = wavelength;

δ = wave discrepancy;

δ_{cr} = wave crests discrepancy;

δ_{tr} = wave troughs discrepancy;

δ_{ph} = wave phase discrepancy;

a = reference level;

d_{50} = median grain size;

g = gravitational acceleration;

i, j, k = indices representing directions along the x-, y- and z-axis;

k_s = equivalent sand roughness;

k = turbulent kinetic energy;

h = still water level;

n = sediment porosity;

η_r = reflected wave amplitude;

η_m = actual free surface elevation;

p = pressure;

s = specific density;

t = time;

u = horizontal velocity;

v = vertical velocity;

z = bed-level;

D = pipeline diameter (m);

E = entrainment rate;

H = wave height;

KC = Keulegan-Carpenter number;

NWT = numerical wave tank;

S/D = normalised maximum scour depth;